CHARACTERIZATION OF THE THERMO-MECHANICAL BEHAVIOR OF CROSSLINKED SILICA AEROGEL

By

ATUL RAMESH KATTI

Bachelor of Engineering

University of Pune

Pune, India

August 2001

Submitted to the Faculty of the
Graduate College of the
Oklahoma State University
in partial fulfillment of
the requirements for
the Degree of
MASTER OF SCIENCE
December, 2005

CHARACTERIZATION OF THE

THERMO-MECHANICAL BEHAVIOR OF

CROSSLINKED SILICA AEROGEL

Thesis Approved:

Dr. Hongbing Lu

Thesis Adviser

Dr. Samit Roy

Dr. Ronald Delahoussaye

Dr. A. Gordon Emslie

Dean of the Graduate College

ACKNOWLEDGEMENTS

I would like to express my gratitude to my parents Mr. Ramesh Katti and Mrs.Sumedha Katti for helping me reach this point in my life. I have been fortunate enough to have good education because of their efforts. I would also like to thank my little sister Ektu for her love and help.

I would like to express my sincere thanks to my advisor Dr. Hongbing Lu for his guidance, both in academics as well as research, for his generous financial support and for teaching a lot of other things. I would like to thank Dr. Samit Roy for the silica aerogel project, for his technical guidance and for serving on my committee. I would like to express my appreciation for Dr. Delahoussaye for serving on my committee.

I would like to thank Dr. Nicholas Leventis at Glenn center, NASA for the support of this project (NASA Grant no: NNC04GB54G) and also for his technical guidance and valuable feedback on the results. I would like to thank Dr. Huiyang Luo for helping me set up the split Hopkinson pressure bar and for his guidance in the experiments. I would like to thank Dr. Brian Grady at University of Oklahoma, Norman for allowing me to conduct experiments on his DMA analyzer and for his help during the experiments.

I would like to thank my colleague Mr. Nilesh Shimpi for working with me on this project and for his friendship and moral support. I would also like to thank Mr. Gang Huang and Mr. Jin Ma for helping me with the nanoindentation experiments, Jerry,

Anand and Rob for various reasons. Finally, I would like to thank the School of Mechanical and Aerospace Engineering here at OSU for allowing me to pursue my MS degree.

TABLE OF CONTENTS

LIST OF TABLES

LIST OF FIGURES

CHAPTER 1

INTRODUCTION

1.1 Silica aerogels

The endeavor for developing strong lightweight materials began long time back. Such materials are very important for aircrafts and spaceships where there is a restriction on the payload capacity. Silica aerogels appear very attractive for such applications due to their low density and high specific stiffness and high specific compressive strength. Nanostructured silica aerogels are chemically inert, highly porous materials. They are the product of sol-gel process whose final step involves extracting the pore-filled solvent with liquid carbon-dioxide. Aerogels have a mass density lower than air and have been considered for aerospace applications such as thermal insulation, catalyst supports, or as hosts for a variety of functional materials for chemical, optical, and electronic applications.

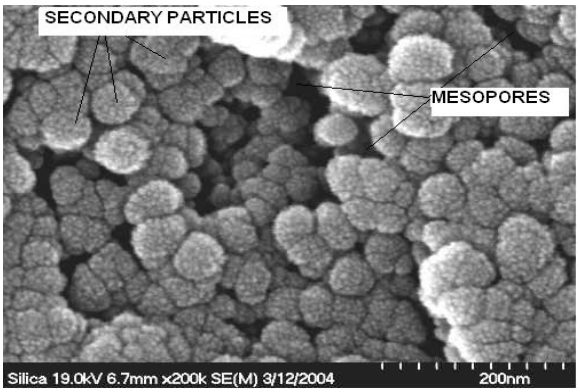

Figure 1.1: SEM image of plain silica aerogel.

Practical applications have been slow though, because aerogels are brittle and hygroscopic, absorbing moisture from the environment which eventually leads to collapse due to capillary forces in the pores. Thus, their use in structural applications presents a challenge. Currently, attention is being placed on improving the mechanical properties of aerogel without sacrificing other unique properties. Base-catalyzed silica aerogels, with an SEM image of the nanostructure shown in figure 1.1, consist of large voids called mesopores (~50 nm) in a "pearl necklace" of microporous secondary particles. These secondary particles are connected by "necks" formed by dissolution and re-precipitation of silica during aging. Consequently, it is reasonable to assume that the mechanical strength of monolithic aerogels can be improved by making the necks wider.

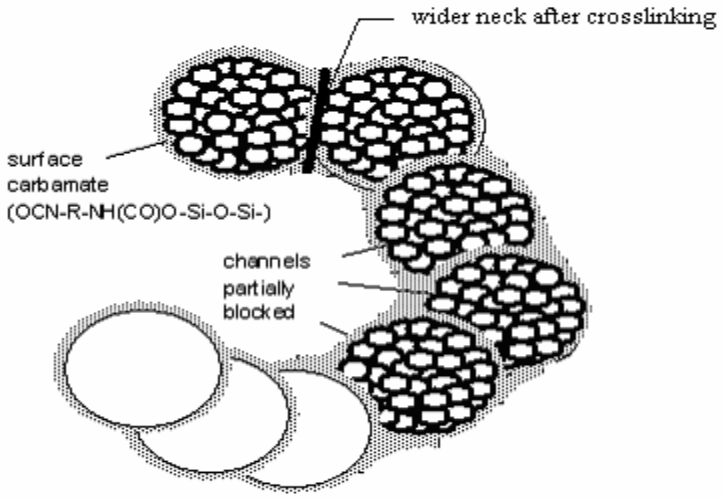

Figure 1.2: Crosslinked aerogel morphology [1].

Leventis [1] accomplished this by using the contour surface of the silica as a template for the deposition and growth of an inter-particle crosslinker. The strength of silica aerogel monoliths was improved by a factor of 100 by crosslinking the aerogels with poly (hexamethylene di-isocyanate). The crosslinked aerogel morphology is shown in figure

1.2. When submerged in liquid nitrogen, plain aerogels absorbed approximately 6.5 times their own weight, of LN_2 and had no structural integrity and collapsed, whereas the crosslinked aerogels when submerged in liquid nitrogen absorbed less than 1.7 times their own weight of LN_2 and did possess considerable structural integrity.

Aerogels with various crosslink densities such as 4%, 8%, 16%, 25%, 34%, 42% and 51% were made by Leventis et al [1]. Three point bending tests on cylindrical specimens were performed to characterize the flexural behavior. The average density of plain aerogel is 0.33 g/cc. The average density of a crosslinked silica aerogel (CSA) is ~0.4 gm/cm^3, but can be made to be as low as 0.03 gm/cm^3, depending on crosslink density. The nanoscale (5-10 nm diameter) secondary particles in silica aerogel are connected by "necks" formed by dissolution and reprecipitation of silica during aging. Improvement in specific stiffness and specific strength of silica aerogel would largely depend on making these necks wider without incurring weight penalty and without sacrificing flexibility. CSA exhibits viscoelastic behavior and so dynamic mechanical analysis (DMA) was done in an attempt to characterize its viscoelastic behavior. The motivation to conduct nanoindentation experiments on CSA was to determine homogeneity, creep compliance and the variation of modulus of CSA with density, and hence these experiments were conducted on samples with three different densities and for each sample the experiments were carried out at an average of four different locations. CSA is a foam material and absorbs a lot of energy before compressive failure. Aerogels can be used as shock absorbers. They have been contemplated for capturing the cosmic dust in the near future. So the impact properties of CSA are of importance in this case and hence high strain testing using a split Hopkinson pressure bar was done.

1.2 Dynamic mechanical analysis

Dynamic mechanical analysis (DMA) experiments are used to study a material's response to an oscillating load. An elastic material will have an instantaneous response to the applied sinusoidal load since it absorbs all the energy, whereas a viscous fluid will have a response (displacement) that is out of phase with the applied force by an angle of $\pi/2$. A viscoelastic material is both viscous and elastic, meaning some part of the energy is dissipated and the rest is absorbed. So the phase difference between the applied load and the displacement of the material is between 0 and $\pi/2$. Greater the phase angle, greater is the viscosity in the material. DMA is an experiment to quantify the absorption and dissipation of the energy. A sinusoidal load is applied on the specimen and the phase lag and the deformation are measured.

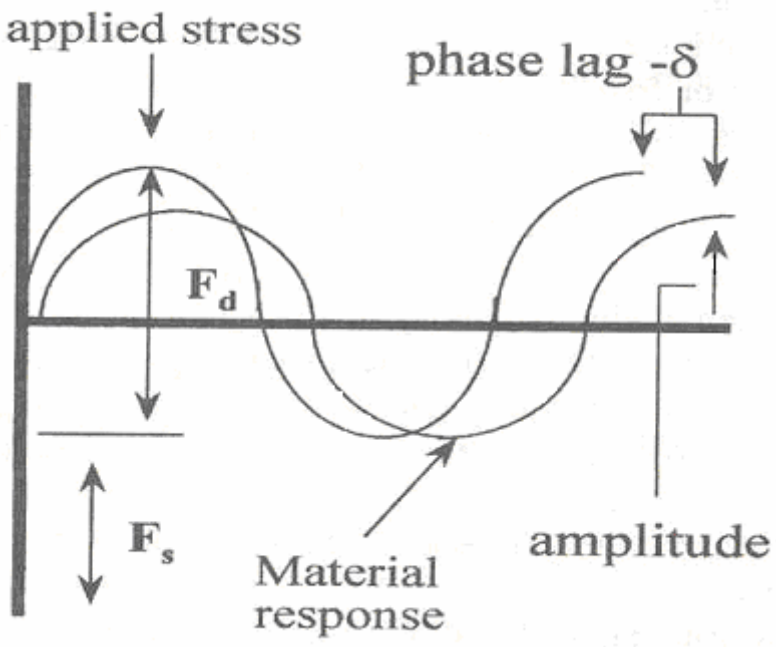

Figure 1.3: Typical stress vs strain curve for a DMA test [2].

As shown in figure 1.3 F_d is dynamic oscillatory force while F_s is the static or clamping force. The force, displacement and phase angle are used to determine the complex modulus, storage modulus and loss modulus.

Figure 1.4 shows the relationship between complex modulus (E*), storage modulus (E'), loss modulus (E") and loss tangent (tan δ) computed from the out-of-phase angle (δ).

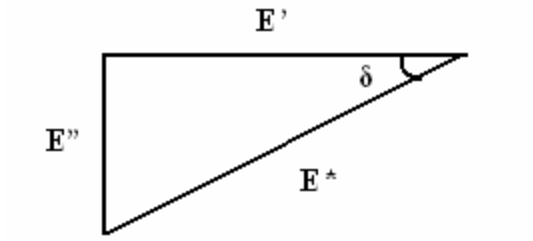

Figure 1.4: Complex, storage, loss modulus and phase angle.

$$E^* = E' + iE'' \tag{1.1}$$

$$\tan(\delta) = \frac{E''}{E'} \tag{1.2}$$

1.3 Nanoindentation

Mechanical characterization on the nanoscale has attained a lot of importance during the past few decades. The conventional macroscopic tests such as tensile testing cannot be used for very small amounts of materials such as MEMS, nanocoatings etc. Instrumented-indentation testing (IIT) or nanoindentation is one of the few methods to accomplish this characterization. Nanoindentation is essentially carried out by penetrating the tip of an indenter into the surface of the material under study. The important condition

for this is that the indenter be harder than the material. As the indenter is driven into the material surface, the material undergoes local elastic and plastic deformation, and as a result an impression is formed on the material surface. The impression geometry is same as the tip geometry. When the indenter is withdrawn, the elastic deformation is recovered and from this the elastic properties of the material can be determined.

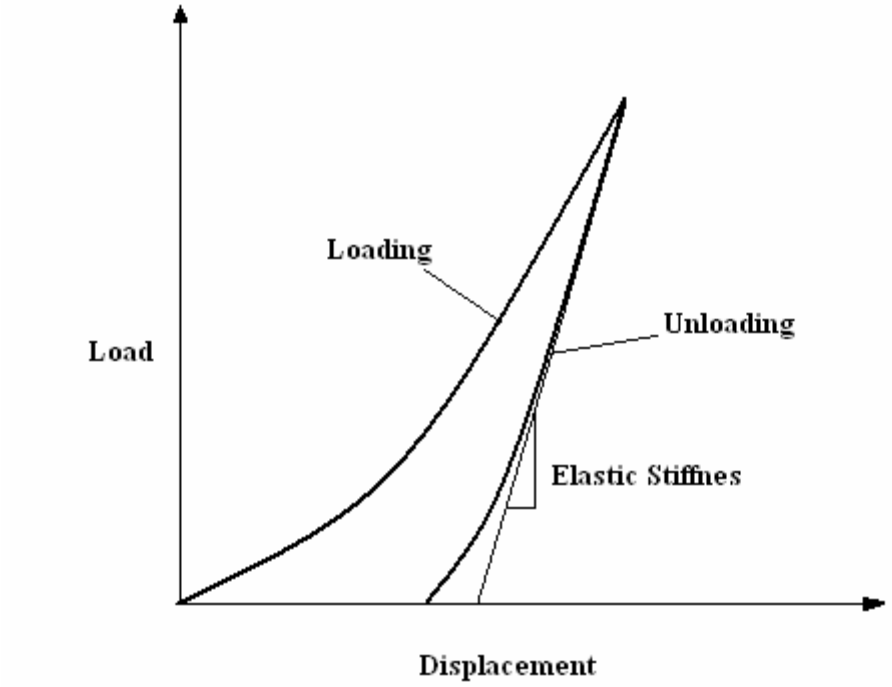

Figure 1.5: Typical load-unload curve for nanoindentation.

Figure 1.5 shows a typical load-displacement curve for a nanoindentation test. As the indenter indents into the surface, the load increases. As the material is unloaded, the load goes down and returns to zero and the slope of the linear part of the unloading curve gives the elastic stiffness. The indenter has a specific geometry at the tip. In nanoindentation the area of the dent is measured from the depth of the indentation and the geometry of the tip of the indenter. Some of the properties that can be measured are hardness, elastic modulus, creep compliance etc. The loads experienced in these tests are

on the order of μN-mN. Figure 1.6 shows the geometry of Berkovich and spherical indenters. A Berkovich indenter is normally modeled as a conical indenter, as shown in the right of the figures in the second row in figure 1.4.

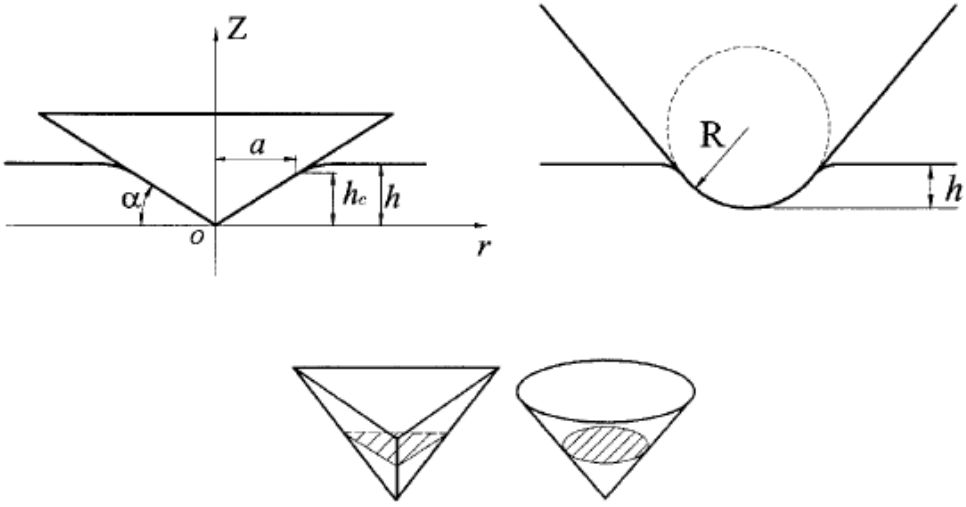

Figure 1.6: Geometry of Berkovich and spherical indenters [3].

While the nanoindentation techniques for measurements of mechanical properties such as Young's modulus and hardness are established, the nanoindentation techniques for viscoelastic materials are still under investigation. Recently, Lu et al [3] developed the following viscoelastic relation (equation (1.3)) between the depth of indentation and the load for ramp loading using a Berkovich indenter, incorporating the prony series parameters of equation (1.4).

$$h^2(t) = \frac{1}{4}\pi(1-\nu)\tan\alpha\left[\left(J_0 + \sum_{i=1}^{N} J_i\right)P(t) - \sum_{i=1}^{N} J_i(\upsilon_0\tau_i)(1-e^{-(P(t))/(\upsilon_0\tau_i)})\right] \quad (1.3)$$

$$J(t) = J_0 + \sum_{i=1}^{N} J_i(1-e^{\frac{-t}{\tau_i}}) \quad (1.4)$$

where h is the indentation depth, α is the angle between the generator of the axisymmetric cone and the flat surface of the workpiece when the Berkovich indenter is modeled as a conical indenter, J_0 and J_i are the compliance numbers, N is the number of terms in the prony series, P is the indentation load, υ_0 is the loading rate and τ_i are the retardation times. Equation 1.1 can be fitted in the experimentally measure load-depth curve using a non-linear least square correlation technique. The prony series parameters can thus be optimized and can then be substituted in equation 1.2 to obtain the creep compliance curve.

1.4 The split Hopkinson pressure bar

The split Hopkinson pressure bar (SHPB) is an apparatus to test materials at high strain rates (~ 10^4 s^{-1}). The following figure shows the schematic of SHPB. Gama et al [4] have reviewed various aspects of SHPB techniques.

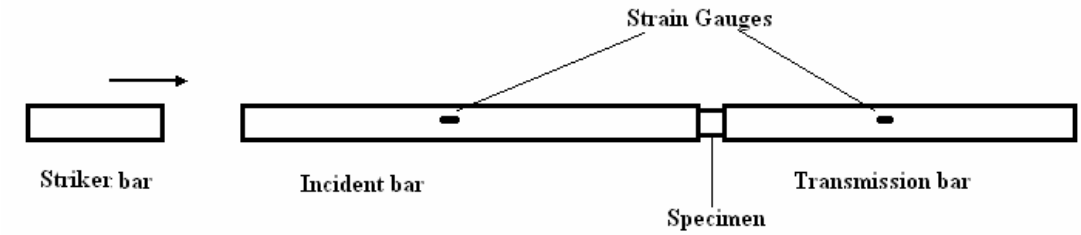

Figure 1.7: Schematic of a split Hopkinson bar.

From figure 1.7 it can be seen that the apparatus primarily consists of three bars, the striker bar, the incident bar and the transmission bar. Strain gauges are mounted on the incident and the transmission bars. The sample is placed between the incident and the transmission bars. Small amount of grease is applied on both the end surfaces of the sample so as to hold the sample intact and to reduce the friction. The operation of the apparatus is as follows. The striker bar is loaded inside the barrel of a gas gun. Air is

filled until specific pressure builds up inside the gas gun. The gas is released using a switch. This launches the striker bar, which in turn impacts on the incident bar. At that moment, a rectangular compression pulse emanates from the end of the incident bar and travels along the length of the bar. When the pulse reaches the interface between the incident bar and the specimen, a part of the wave is reflected back as a tensile pulse and the remaining part is transmitted through the specimen into the transmission bar. These three pulses, the incident pulse, reflected pulse and the transmitted pulse are used for one dimensional wave analysis to measure the strain and stress in the specimen. Strain gauges mounted on the incident bar measure the incident and the reflected pulse, whereas the ones mounted on the transmission bar measure the transmitted pulse. Alignment of the bars is a critical factor. The incident and the transmission bars are supported by plates on the main frame. Each strain gauge forms the part of Wheatstone bridge. When the wave passes the location of the gauges, the output voltage change in the bridge is proportional to the resistance change of the gauges. Typically, high frequency oscilloscopes (> 10 MHz) are used to record the voltage as a function of time. Kolsky [5] developed the following relation for the stress in the specimen.

$$\sigma(t) = \frac{A_b E \varepsilon_T(t)}{A_s} \tag{1.5}$$

Where E is the Young's modulus of the transmission bar, A_b is the cross sectional area of bar. Equation 1.5 was developed using one-dimensional wave analysis and is valid only if the sample is in dynamic equilibrium and is loaded with constant strain rate. The wave speed in the incident bar can be calculated using the following relation.

$$c = \sqrt{\frac{E}{\rho}} \tag{1.6}$$

where E is the elastic modulus of the bar and ρ is the density. The strain rate in the specimen can be calculated from

$$\dot{\varepsilon}_s(t) = -\frac{2c}{L}\int_0^t \varepsilon_r(t)dr \qquad (1.7)$$

where $\varepsilon_R(t)$ is the strain history of the reflected wave, L is the original specimen length and c is the wave speed calculated from equation 1.6.

Equation 1.7 can be integrated to obtain the strains in the specimen at various times. After the conditions for dynamic equilibrium are reasonably satisfied, the data can be processed to obtain a stress strain curve at high strain rates.

1.4.1 Problems with split Hopkinson pressure bar testing

The voltage signal from the Wheatstone bridge is small, on the the order of mV. So the surrounding voltage noise can easily interfere with this voltage and it may thus be difficult to determine the actual signal. Hence proper care has to be taken in terms of isolating and shielding all the electrical devices.

Alignment is a critical issue; a misaligned Hopkinson bar may give rise to bending and may obstruct the movement of the bars. This affects the waves traveling through the bar. Hence alignment has to be thoroughly checked.

Equations (1.5) and (1.7) are only valid if the specimen is in dynamic equilibrium when it is loaded. Soft materials have low impedance and it may be difficult to obtain dynamic equilibrium and hence the equations will be invalid. In such cases normally a pulse shaper is used to shape the pulse and to achieve the desired effect. Obtaining a constant strain rate may also be an issue.

CHAPTER 2

REVIEW OF LITERATURE

2.1 Silica aerogel

2.1.1 History

The following history is taken from a compilation by Arlon Hunt and Michael Ayers [6]. Silica aerogels were first prepared by Steven Kistler in 1931. In an endeavor to separate the liquid from a wet gel, Kistler tried to dry the wet gel. There was some shrinkage accompanied by cracking. Kistler surmised that the solid part of the gel had micro pores and that the evaporating liquid exerted strong surface tension on the pore structure and hence the later collapsed. Hence Kistler thought of replacing the liquid part of the gel with “air” and hence the name “aerogel” was coined by him and the reason is evident in the following line taken from one of Kistler’s papers.

"*Obviously, if one wishes to produce an aerogel, he must replace the liquid with air by some means in which the surface of the liquid is never permitted to recede within the gel. If a liquid is held under pressure always greater than the vapor pressure, and the temperature is raised, it will be transformed at the critical temperature into a gas without two phases having been present at any time*." (S. S. Kistler, *J. Phys. Chem.* **34**, 52, 1932). Kistler had several failures in the beginning, one of them being his attempt to prepare aerogels by the acidic condensation of aqueous sodium silicate. When he tried to convert

the water in the gels to a supercritical fluid, the supercritical water dissolved the silica, which precipitated later. Kistler then washed the silica gels with water and then exchanged the water with alcohol. He then converted the alcohol to a supercritical fluid and allowed it to escape and thus aerogels were prepared. These aerogels had a low density and were highly porous and transparent. Kistler thoroughly characterized these gels in the next several years. Aerogels were almost forgotten till the late 1970s when the French government approached Stanislaus Teicher at Universite Claud Bernard for developing a method for using porous materials to store oxygen and rocket fuels. The research conducted over there eventually lead to a revolution in the field of aerogels. Sol-gel chemistry was used in the preparation of aerogels. In this process, the sodium silicate used by Kistler was replaced by an alkoxysilane called tetramethoxyorthosilicate (TMOS). The hydrolysis of TMOS in a solution of methanol produced "Alcogel" in one step. This process had the advantage that the water-to-alcohol step was eliminated and also the inorganic salts in the gel. High quality silica aerogels were produced by drying these alcogels under supercritical alcohol conditions. A variety of metal oxide aerogels were produced after this. There were a lot of advances in this field after this. In the early 1980s silica aerogels prepared by the TMOS method were used as a medium for the production and detection of Cherenkov radiation. Members of the Lund group in Sjobo, Sweden set up a plant for the production of silica aerogel monoliths using TMOS. The plant had a 3000 liter autoclave designed for handling supercritical methanol that developed a leak and the room containing the vessel exploded. The plant was later rebuilt and it continues to produce silica aerogels. In 1983 Arlon Hunt and the 'Microstructured Materials Group' at Berkeley lab replaced TMOS with tetraethylorthosilicate (TEOS), a

much safer reagent, and that the alcohol within a gel could be replaced by liquid carbon dioxide before supercritical drying without harming the aerogel. The critical point of CO_2 (31 degrees C and 1050 psi) occurs at much less severe conditions than the critical point of methanol (240 degrees C and 1600 psi) and CO_2 is not vulnerable to explosion as is methanol. "BASOGEL" was produced by developing CO_2 substitution methods for the preparation of silica aerogel beads from sodium silicate by BASF in Germany. This material was produced only until 1996. In 1985 Prof. Jochen Fricke organized the first international symposium on aerogels (ISA) in Wurzburg, Germany. Since then there have been six more ISAs held (1988, 1991,1994,1997,2000 and 2003). The lowest density aerogels (0.003 g/cm^3) were prepared by Larry Hrubesh in the late 1980s, at Lawrence Livermore National Laboratory (LLNL). This density was three times that of air. Rick Pekala, also of LLNL, made efforts to prepare aerogels of organic polymers. These included resorcinol-formaldehyde, melamine-formaldehyde aerogels. Efforts were made to eliminate the supercritical drying step by chemically modifying the surface of gel prior to drying at the University of New Mexico.

2.1.2 Structure of aerogel

Wang et al [7] studied the crystal structure of carbon doped silica aerogel by laser ablation time-of-flight mass spectrometry. Figure 2.1 shows a nanostructure of silica aerogel proposed by Wang et al. The researchers concluded that silica aerogels have a clustered structure and the smallest units are the primary particles that have a diameter of one nanometer or less, and they have the same density as ordinary, nonporous glass. The primary particles are made of silicon, hydrogen and oxygen atoms. Two silicon atoms are

bridged by oxygen atoms and silicon atoms tend to bond four oxygen atoms wherever possible. These particles together form a secondary particle, whose density is half that of glass. The secondary particles have a radius of the order of five-ten nanometers. So, considering the sizes of the primary and secondary particles it is reasonable to assume that one secondary particle consists of at least 100-125 primary particles. The secondary particles are strung out in chains to create the delicate and extremely porous silica aerogel skeleton, whose density is typically 5 percent that of ordinary glass.

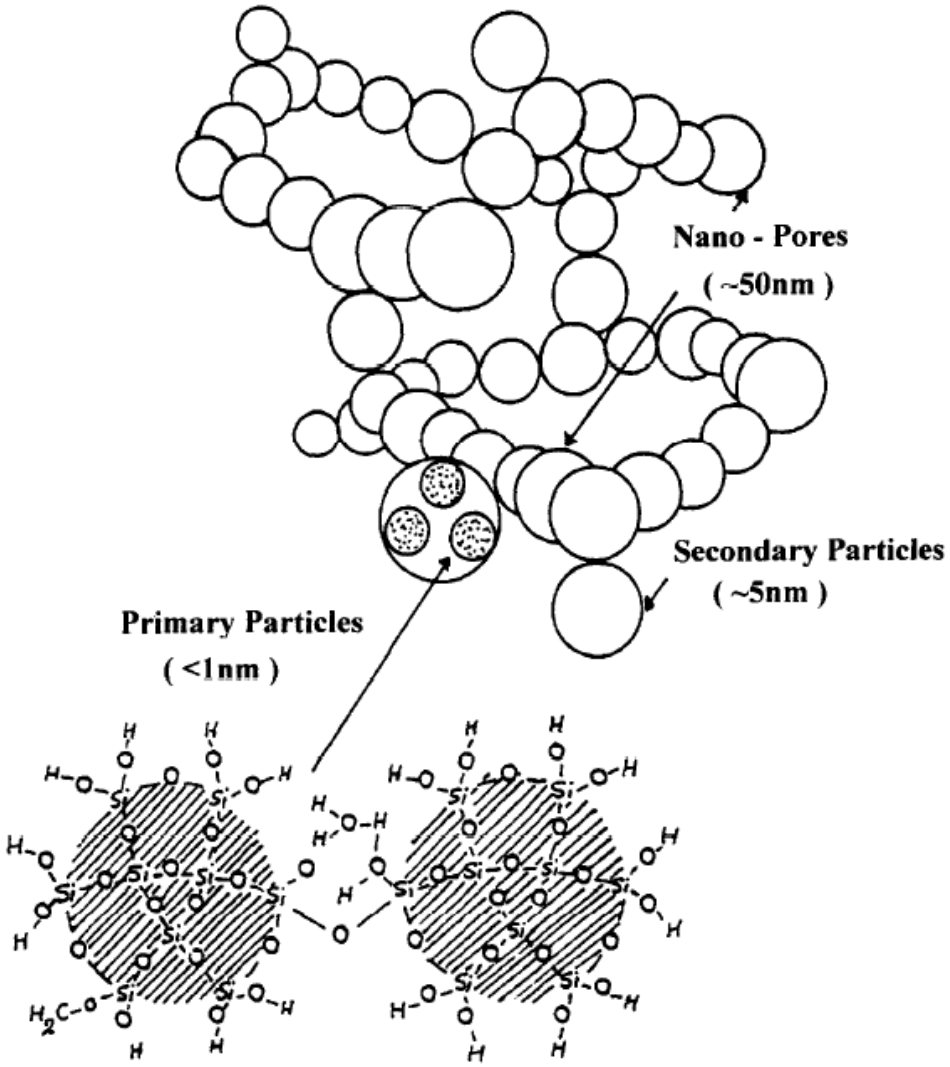

Figure 2.1: A proposed structure of silica aerogels [7].

2.1.3 Improvement of mechanical properties of silica aerogel

Aerogels have been found feasible to capture hypervelocity projectiles relatively intact [8]. Dominguez et al [9] proposed and tested a model of compaction driven impact cratering in aerogels. The model derives impact crater dimensions directly from energy and momentum deposition.

Aerogels have been contemplated for thermal applications [10], catalyst supports [11], and for optical, electronic and chemical applications [12]. The mechanical properties of silica aerogels obtained from the sol-gel process are not well suited for a lot of applications since they are brittle and hygroscopic [13]. In 2002, Leventis et al [1] devised a method to cross link silica aerogel in a quest for obtaining stronger lightweight materials.

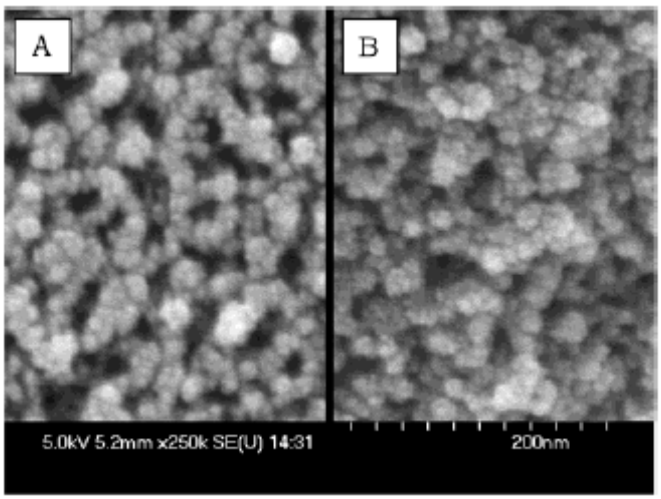

Figure 2.2: SEM images of fractured monoliths of a native silica aerogel (A) and a di-ISO cross-linked silica aerogel [1].

Poly (hexamethylene diisocyante) was used to crosslink the aerogels. The crosslinked aerogels had a considerable increase in strength, were less hygroscopic and did not collapse when in contact with liquid. As seen in figure 2.2A, the so called secondary particles are connected by necks formed by dissolution and reprecipitation of silica during aging. Figure 2.2B shows that the necks have been made wider by the addition of poly (hexamethylene diisocyante) (di-ISO). The di-ISO surrounds the secondary particles. Since several secondary particles appear fused, the mesoporocity is somewhat reduced. Leventis et al found that the composite monoliths (cross-linked silica aerogel) are stronger and less hygroscopic than the native silica aerogels.

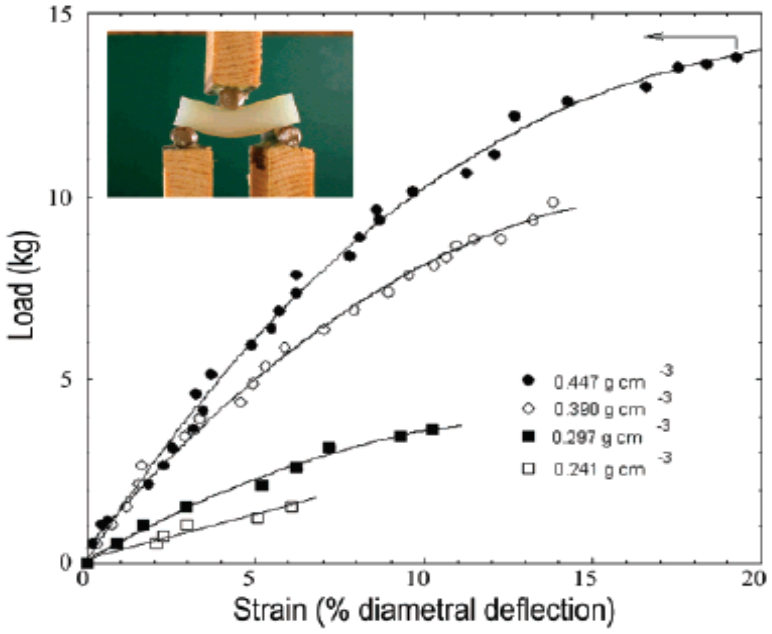

Figure 2.3: Load-strain curves for four composites of different densities. The arrow correlates the particular data point with the image in the inset (bending under 14.4 kg load of the monolith with density 0.447 g cm-3; span is 1.738 cm) [1].

When native silica aerogels were submerged in liquid nitrogen, they absorbed moisture almost 6.5 times of their weight. They underwent intensive cracking and lost structural integrity completely. Cracking was also observed in lighter composites but the mode of fracture was different and they exhibited better structural integrity.

It was also determined that the rupture load required in three point bending of the cylindrical samples was 100 times more for the cross-lined aerogel samples(density 0.447 g/cc) (~15 Kg) than that required for the native silica aerogel monolith.

Figure 2.3 shows the complete load-deflection curves for four cross linked aerogels of different densities, for three-point bending experiments conducted by Leventis et al. It can be seen from the figure that the least dense sample is nearly linearly elastic. The more dense samples exhibit nonlinear behavior.

2.2 The split Hopkinson pressure bar (SHPB)

2.2.1 Historical background

The split Hopkinson bar gets its name from John Hopkinson, who in 1872 determined the properties of iron wire by dropping a weight on the wire and by measuring the deformation it underwent. In 1914 his son, Bertram Hopkinson introduced a technique for determining the pressure developed during an impact produced by a bullet. He used a ballistic pendulum method for determining the shapes of pulses caused by the impact of bullets or the detonation of explosive charges at one end of a long rod. The apparatus consisted of a long rod suspended by two sets of wires. A small rod was placed at the end of this rod. The long rod was impacted by a bullet and a compressive wave traveled along the axis of the bar and then into the short bar. This short bar flew off and was caught by a

box that was suspended. The momentum of the box was calculated by using a simple displacement device. In 1941 Bancroft solved bar frequency equation by Pochhammer and Love to determine the velocity of longitudinal waves in the bars. In 1948 Davies improved the measurement method by using condensers. The condensers were used to measure the displacement and hence the pressure. The use of condensers improved the measurement process and also the results. In 1949 Kolsky introduced another bar and that is how the apparatus got its name as *split* Hopkinson bar. It is also known as Kolsky bar. Microphones were used in the second world war to interconvert mechanical and electromagnetic energy, hence he used condensers microphones to measure the strain history from both the bars.

2.2.2 Some issues with testing

The equations mentioned in section 1.3 are only valid if the sample is in dynamic equilibrium state during testing. Yadav et al [14] determined that the data for the compressive flow stress of metals are usually obtained for strains larger than few percent as elastic and early yield behavior cannot be captured properly by this technique. This could be a major problem while testing brittle materials, as most of the material behavior occurs at lower strains. A steeply rising incident pulse can destroy the brittle material without achieving dynamic equilibrium and may also cause dispersion effects [15-16]. Franz et al [15] and Follansbee [16] have discussed the importance of shaping the pulse to obtain a slowly rising pulse to avoid the effects mentioned above. They conducted some experiments using a pulse shaper. They used materials such as paper, aluminum, brass etc. The pulse shapers are usually chosen by a trial and error procedure. To eliminate high frequency oscillations, Wu and Gorham [17] used paper on the impact

surface of the incident bar. Togami et al [18] used a thin plexiglass disk to reduce the dispersion in the bar. For elastomer specimens, Chen et al [19] used a polymer disk as the pulse shaper. Striker bars with truncated cones were used by Christensen et al [20] to produce ramp pulses. Frew et al [21] obtained an expression for the thickness of the pulse shaper and presented results for both hard and annealed C11000 copper pulse shapers.

For a soft material, the transmitted signal is small. Chen et al [22] used a piezoelectric transducer on the transmission bar, instead of a strain gauge to measure the weakly transmitted force from soft specimens like elastomers and foams.

CHAPTER 3

AEROGEL PREPARATION AND DYNAMIC MECHANICAL ANALYSIS

3.1 Preparation of crosslinked silica aerogel

Acetonitrile, tetramethoxyorthosilicate (TMOS) and 3-aminopropyltriethoxysilane (APTES) were purchased from Aldrich and were used as received. Desmodur N3200 hexamethylene diisocyanate oligomer was obtained courtesy of Bayer Corporation (Pittsburgh, PA).

The procedure for preparation of cross linked aerogel (CSA) as developed by Dr Leventis at Glenn center research, NASA was used in CSA preparation.

In a typical procedure as shown in figure 3.1, two solutions, one containing 3.8 mL TMOS, 1.3 mL APTES and 4.5 mL CH_3CN (solution A), and another one containing 4.5 mL CH_3CN and 1.5 mL water (solution B) were cooled in a dry ice/acetone bath and were mixed rapidly by adding solution B into solution A. The resulting sol was shaken vigorously and was divided into appropriate molds. (As molds for the cylindrical samples used in compression testing we employed 19.6 mm diameter, 20 cc polyethylene syringes, and for the square cross-section samples used in the three-point flexural bending testing we used 12.7 mm x 12.7 mm square cross-section plastic tubes.) Gelation takes place once the temperature reaches about room temperature (< 1 min). Gels were allowed to stand (age) for 2 h and subsequently they were removed from their

molds and placed in fresh CH_3CN. The washed solvent-to-gel volume ratio was approximately 5:1. The solvent (CH_3CN) surrounding the gel was changed every day for 3 days at ~24 h intervals. Subsequently, the gels were placed in an isocyanate solution containing 32 g of Desmodur N3200 in 80 mL of CH_3CN and were let to equilibrate for 24 h under frequent agitation.

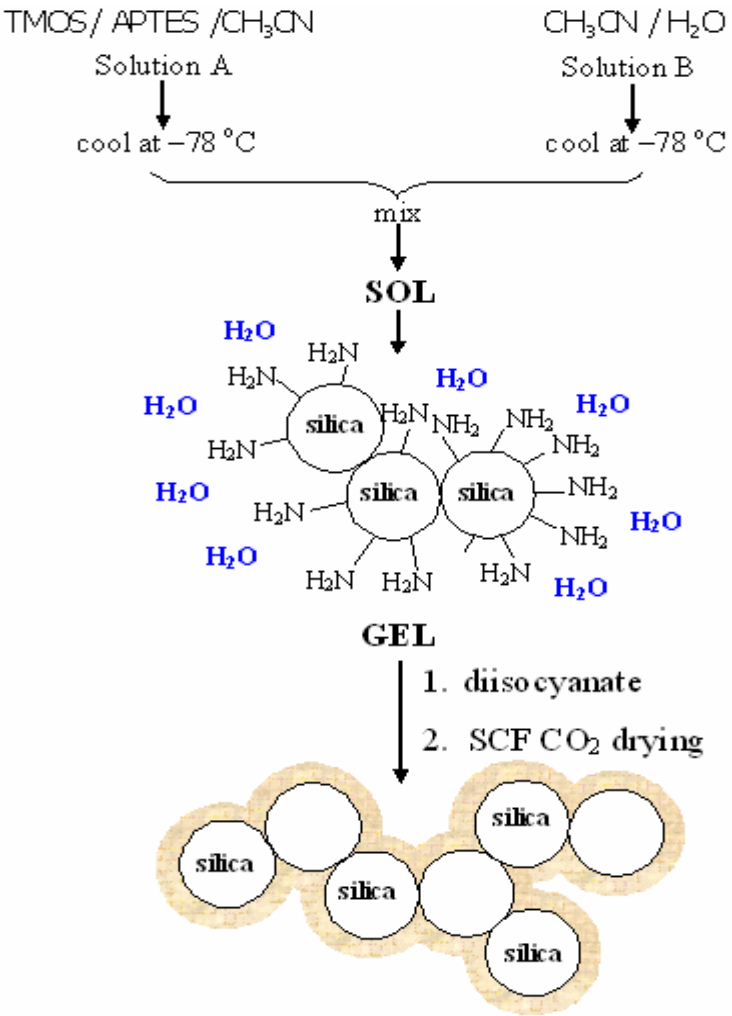

Figure 3.1: Preparation and crosslinking of silica aerogel.

At the end of the period samples were removed from the isocyanate solution and were placed in a new container with fresh CH_3CN and were placed in a 70 ^{o}C oven for 3 days. Next, the containers were let to cool to room temperature and the gels were removed and

placed in fresh CH_3CN, which was changed another three times in 24 h intervals. Finally, the gels were transferred in an autoclave equipped with a 1 L, 3" diameter pressure vessel (Applied Separations Model Spe-edSFE) filled with CH_3CN, and were extracted with liquid CO_2, which was taken out supercritically. Figure 3.2 shows a neat silica aerogel specimen and a crosslinked one.

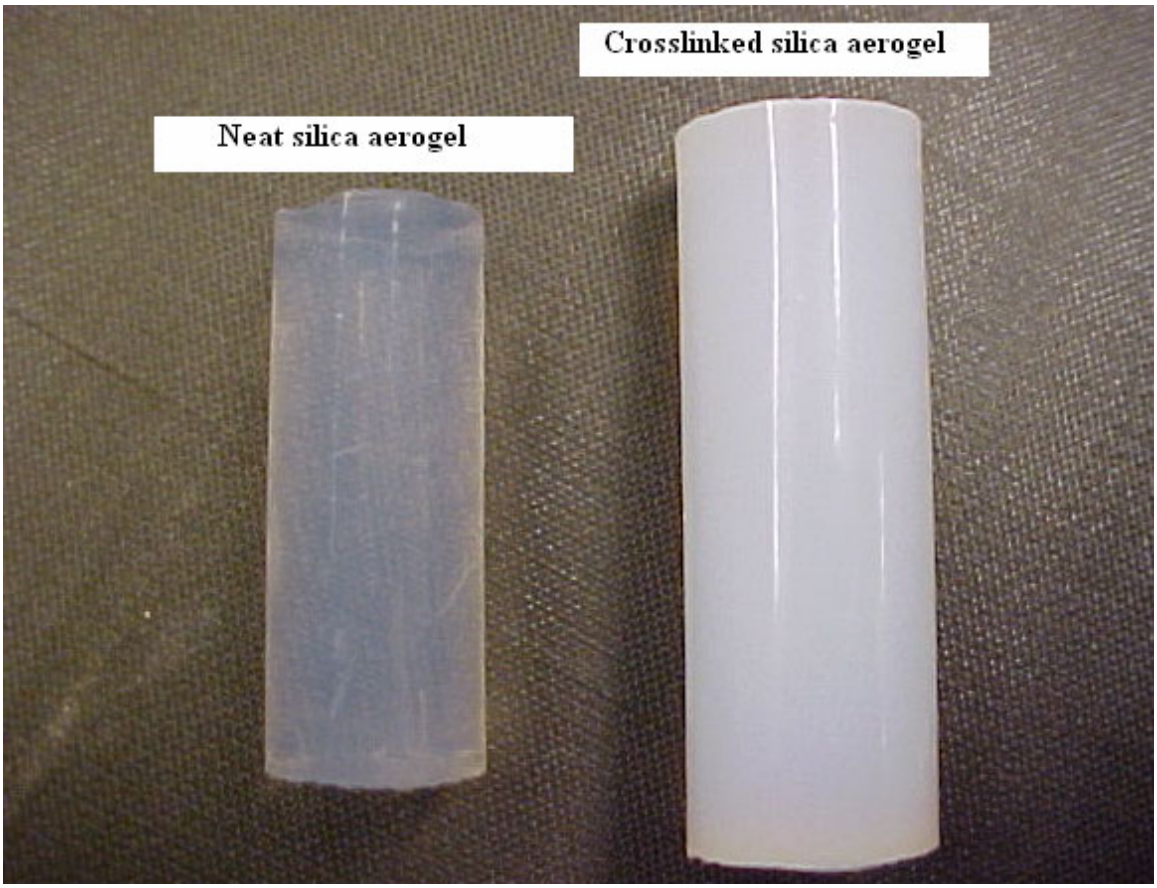

Figure 3.2: Neat and crosslinked silica aerogel.

3.2 Dynamic mechanical analysis

3.2.1 Experimental setup

All the DMA experiments were conducted using the Dynamic Mechanical Analyzer Model RSA II (Rheometric Scientific Inc, Piscataway, NJ) (figure 3.3) at the University of Oklahoma, Norman.

Figure 3.3: DMA setup.

The complex modulus was measured in three-point bending mode on samples with nominal dimensions of 50mm × 8mm × 3 mm .The molds with rectangular cross section 8mm × 3 mm for the DMA samples were custom made by Ace Glass Inc. (Vineland, NJ). Each mold was open at both ends. One end was covered with two layers of parafilm, while the mixture of solutions A and B as described in Section 2.1 was poured from the other end, which was then covered with two layers of parafilm. After aging for two hours, the parafilm layers were removed from both ends and the sample was pushed using a

plastic plunger with the same internal dimensions of the mold. In a DMA test, a sample was supported by two knife edges on a forked fixture separated by a fulcrum span (figure 3.4).

Figure 3.4: Three point bending setup.

A load was applied by moving this fulcrum span against a similar knife edge on top of the middle span of the bending specimen. The DMA test can thus be considered as a beam with pin-pin support loaded by a concentrated force applied in the middle of the beam. The type of DMA test is called temperature sweep. The major purpose for temperature sweep was to determine the glass transition temperatures. To this end, the use of one fixed frequency, 1 Hz in this case, was adequate. The fixture used in this type of test had a span of 29.5mm so that a temperature of 210°C could be reached without the

specimen falling down from the fixture due to shrinkage at elevated temperatures. At 1 Hz, the temperature in the temperature chamber was set to and maintained at -132°C for approximately 60 seconds, data for the sinusoidal load and displacement were acquired by the DMA apparatus. Then temperature was increased to and maintained at the next neighboring temperature for approximately 60 seconds; data representing on the sinusoidal load and displacement were taken at this temperature. This procedure would repeat as temperature was increased up to 210°C. The second type of DMA tests is called frequency sweep. The major purpose of these tests was to determine the complex modulus of CSA as a function of frequency over a range of temperatures. In these tests, the temperature inside the temperature chamber of the DMA apparatus was first set to -130°C, close to the lowest point the chamber could reach. 30 minutes after the temperature has reached -130°C, DMA test would start at a frequency of 16 Hz, then at the same temperature, the DMA tests would run at a decreased frequency of 13Hz, 10Hz, 6Hz, 4Hz, 2Hz, 1Hz, 0.5Hz, 0.1Hz and 0.01Hz. Then temperature was increased to the next neighboring temperature, -97°C, DMA tests using the same frequency sweep as used at -130°C would be conducted. Then temperature would increase again, and DMA tests would run at elevated temperatures until the DMA sample shrank to a length that could not be held by the two edges with a fulcrum span of 48 mm due to negative coefficient of thermal expansion in the CSA material. The temperature at which a sample shrank to a length shorter than 48 mm was 100°C. The temperatures used in these tests were selected in a way such that complex modulus at two neighboring temperatures would overlap if the complex modulus curves as a function of frequency were shifted horizontally. It is noted that in three-point bending tests, a small amplitude sinusoidal load was

superimposed on a concentrated compressive load all the time as frequencies were varied at each temperature. As the CSA bending stiffness changes with temperature, the concentrated compressive load was adjusted carefully so that only infinitesimal deformations were experienced by a sample to ensure that the complex modulus was measured in the regime of linear viscoelasticty.

3.2.2 Results

As mentioned earlier, the CSA samples were tested at a range of temperatures and frequencies. It was noted that CSA sample dimensions change with temperatures; in general CSA sample dimensions decrease with the increase of temperatures.

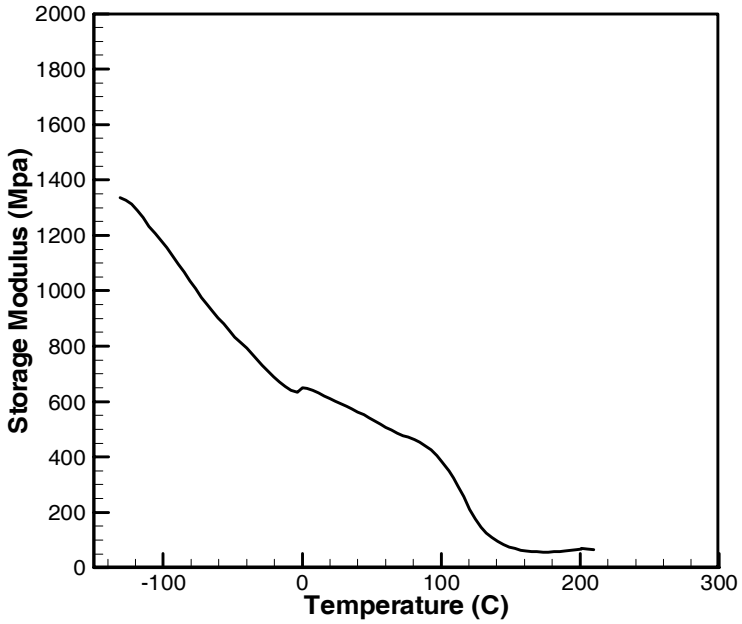

Figure 3.5: Storage modulus for CSA at 1Hz and 0.15 strain.

In the computation of complex modulus as determined from DMA tests, nominal stress and nominal strain were used, so that the complex modulus, with storage modulus as its real part and loss modulus as its imaginary part, should be considered as "nominal"

complex modulus, rather than "true" complex modulus. Figure 3.5 depicts storage modulus as a function of temperature as determined from temperature sweep DMA tests. As shown in the figure, in general the CSA storage modulus decreases with temperature. At room temperature, the CSA storage modulus is 611.2 MPa; at 100°C, its storage modulus is 328.3 MPa. Around 130°C, the storage modulus decreases at a steep rate with temperature, this indicates that α glass transition occurs at 130°C. Above 130°C, the storage modulus shows slight increase. The storage modulus at 210°C is 66.5MPa, about 5% of the modulus at -132°C. Around -50°C, the storage modulus shows a steep reduction as well, indicating a possible glass transition.

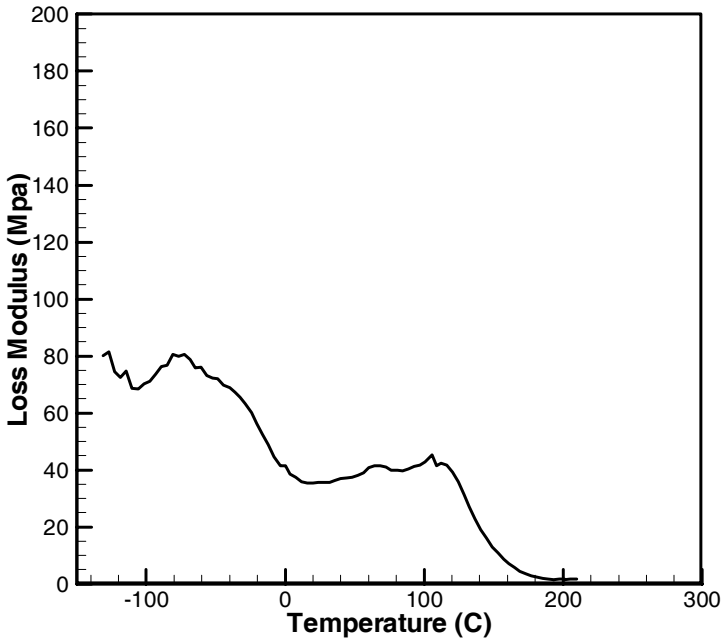

Figure 3.6: Loss modulus for CSA at 1Hz and 0.15 strain.

Figure 3.6 is the plot of the loss modulus as a function of the temperature.

Figure 3.7 presents the out-of-phase angle in radians, δ, between sinusoidal load and sinusoidal displacement. In a typical viscoelastic material, the sinusoidal load is ahead of

sinusoidal displacement by a phase angle between 0 and $\pi/2$. The loss modulus is computed in terms of storage modulus multiplied by tan(δ). In figure 3.7, around 130°C, labeled as A, there is a peak in tan(δ) data. The peak indicates that the CSA has a

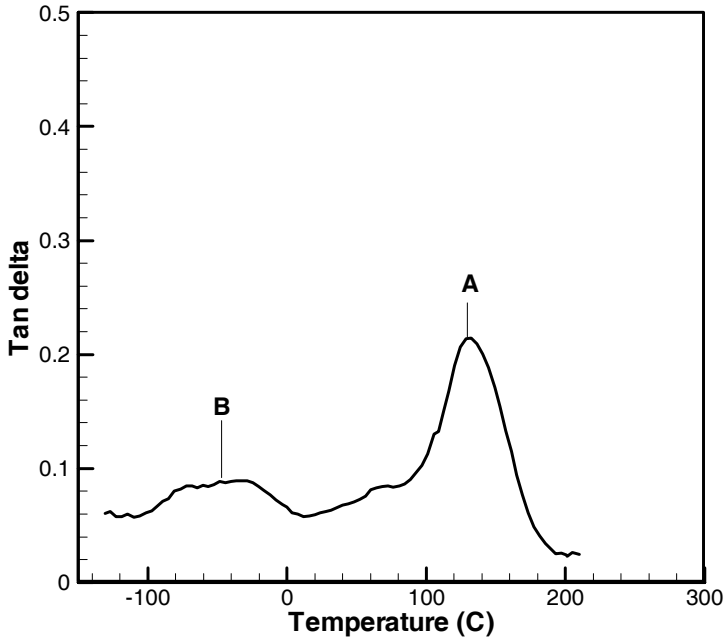

Figure 3.7: Tan Delta for CSA at 1Hz and 0.15 strain.

relatively high viscosity around this temperature, and thus higher energy dissipation, and more pronounced time-dependent behavior due to viscosity. In the presentation of storage modulus earlier, it was found that the CSA storage modulus experienced quickest descent around 130°C. Thus through the reading of both storage modulus and loss modulus of CSA, it can be determined that the major glass transition (called α transition) temperature of CSA is 130°C. A viscoelastic material normally shows very significant time-dependent reduction of modulus when it is used around α glass transition. Consequently, for use of CSA as a structural material, the CSA has to be used well below α glass transition temperature 130°C. In figure 3.7, around -50°C, labeled as B, there is another

peak, indicating a possible transition. This peak corresponds to steep reduction in storage modulus as shown in figure 3.5 around -50°C. Data for both the storage modulus and loss modulus indicate the existence of a secondary glass transition, called β transition.

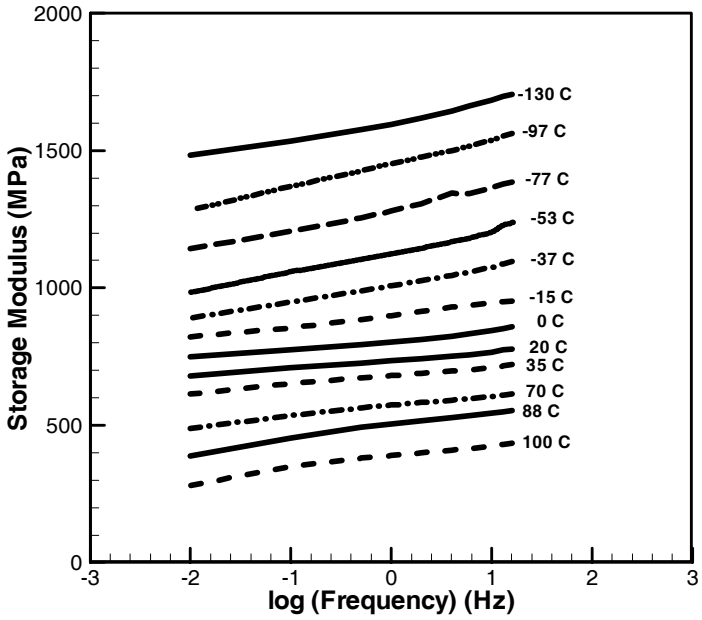

Figure 3.8: Storage modulus for the frequency scan at various temperatures on CSA.

Figure 3.8 shows the storage modulus as a function of frequency as measured from frequency sweep DMA tests. At all temperatures, storage modulus increases with the increase in frequency. Storage modulus curves at neighboring temperatures have similar shapes, consequently, they can be shifted horizontally to form a master curve (figure 3.9) referred to 20°C. The corresponding shift factors are plotted in figure 3.10. The master curve as shown in figure 3.9 could be used to determine the storage modulus over 25 decades in the frequency domain. The loss modulus as a function of frequency is plotted

in figure 3.11. In contrast to the storage modulus curves, the loss modulus curves at some neighboring temperatures do not have the same shape; consequently, they cannot be

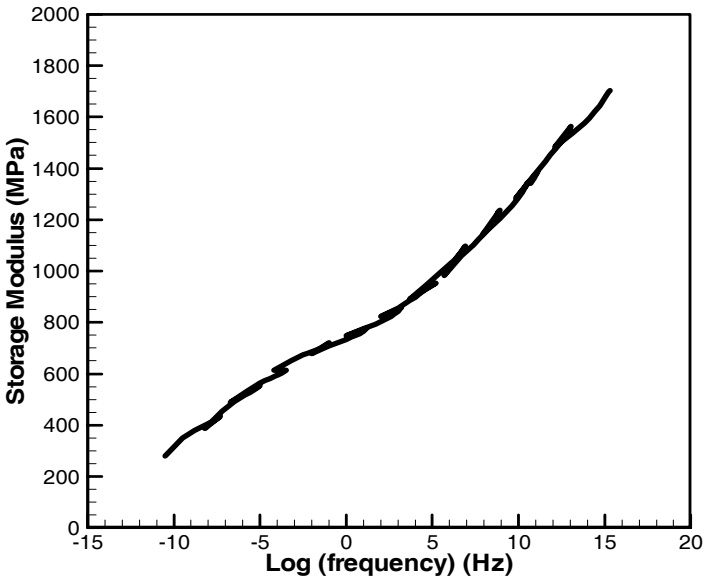

Figure 3.9: Master curve for storage modulus during the frequency scan at various temperatures on CSA, referred at 20^{o}C.

shifted horizontally to form a master curve. This feature indicates that the CSA is a thermorheologically complex material. This might place doubt on the validity of the storage modulus master curve as shifted horizontally from data at different temperatures in figure 3.9.Whether the master curve for the storage modulus is valid or note depends on testing results of CSA at higher or lower frequencies outside the range of frequencies used in DMA tests. This alone is a major endeavor, and will be pursued in the future work.

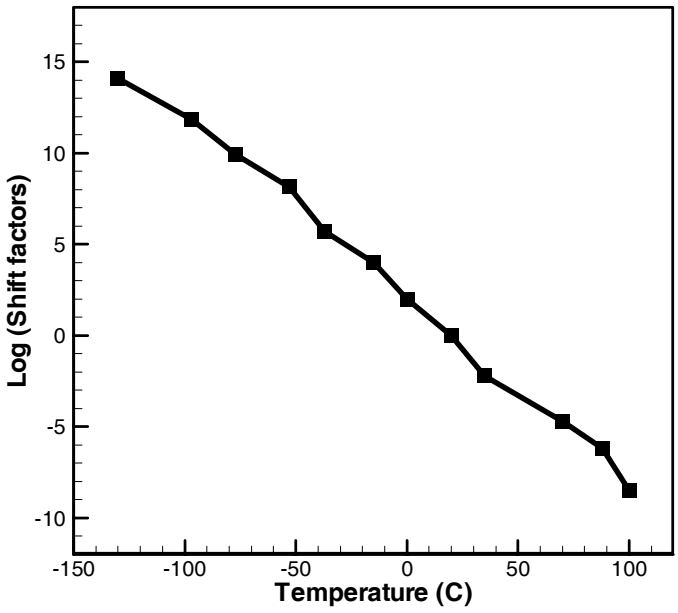

Figure 3.10: Shift factors for the master curve for storage modulus during the frequency scan at various temperatures on CSA, referred at 20^{o}C.

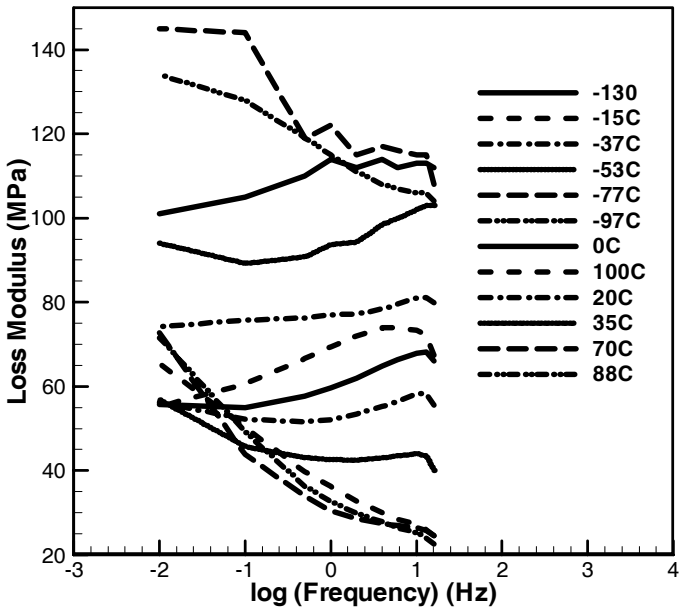

Figure 3.11: Loss modulus for the frequency scan at various temperatures on CSA.

CHAPTER 4

CHARACTERIZATION OF MECHANICAL BEHAVIOR OF CSA AT HIGH STRAIN RATES USING THE SPLIT HOPKINSON PRESSURE BAR

4.1 Theory: Derivation of equations for dynamic equilibrium

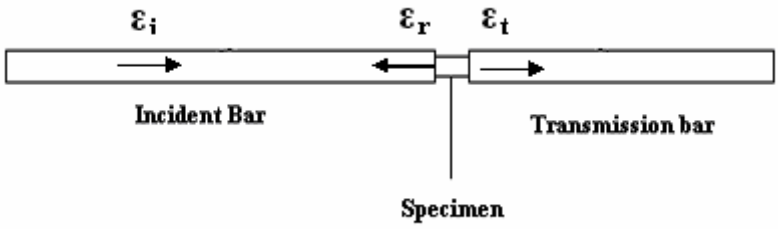

Figure 4.1: Incident, reflected and transmitted waves.

As explained before the Hopkinson bar consists of a striker bar, incident bar and a transmission bar. The sample is sandwiched between the incident and transmission bar. When the striker bar hits the incident bar, a longitudinal wave emanates from left end of the incident bar having a strain value of ε_i. When this wave reaches the interface between the bar and the specimen, a part of it (ε_r) gets reflected back and the remaining part of the wave (ε_i) is transmitted to the transmission bar. The specimen strain rate and the stress can be calculated by performing one-dimensional analysis of these waves.

The one dimensional wave equation is

$$\frac{\partial^2 u}{\partial x^2} = \frac{1}{c^2}\frac{\partial^2 u}{\partial t^2} \tag{4.1}$$

where c is the wave speed in the material.

The solution for equation (4.1) is

$$u(x, t) = f(x-ct) + g(x+ct) = u_i + u_r \tag{4.2}$$

where u_i is the incident wave displacement and u_r is the reflected wave displacement

The strain can be obtained by differentiating the above equation with respect to x. Thus one has,

$$\varepsilon = f' + g' = \varepsilon_i + \varepsilon_r \tag{4.3}$$

The velocity of any point on the incident bar can be calculated by differentiating equation (4.2) with respect to time. Thus,

$$\dot{u}_i = c(-f' + g') = c(-\varepsilon_i + \varepsilon_r)$$

(4.4)

The displacement for the transmitted wave is given by

$$u_t = h(x-ct) ,$$

therefore, $$\varepsilon_t = h'. \tag{4.5}$$

The velocity in the transmission bar is

$$\dot{u}_t = c(-h') = c(-\varepsilon_t) \tag{4.6}$$

The strain rate in the specimen can be calculated by

$$\dot{\varepsilon}_s = \frac{(\dot{u}_t - \dot{u}_i)}{L} = \frac{c}{L}(-\varepsilon_t + \varepsilon_i - \varepsilon_r) \tag{4.7}$$

where L is the length of the specimen.

The forces in both the bars can be determined by the following formulae

$$P_1=AE(\varepsilon_i + \varepsilon_r);\ P_2=AE\ \varepsilon_t \tag{4.8}$$

where A is the area of the bars and E the Young's modulus

It is assumed that the forces P_1 and P_2 are equal since wave propagation effects may be neglected for short specimens and thus from equations (4.8) we have

$$\varepsilon_i + \varepsilon_r = \varepsilon_t \tag{4.9}$$

Substituting (4.11) in (4.9) and integrating the resulting equation with respect to time,we have

$$\varepsilon_s(t) = -\frac{2c}{L}\int_0^t \varepsilon_r(\tau)d\tau \tag{4.10}$$

The stress in the specimen can be calculated by dividing either P_1 or P_2 by the area of the specimen.

$$\sigma_s(t) = \frac{A}{A_s}E\varepsilon_t(t) \tag{4.11}$$

4.2 Experimental test setup

Figure 4.2 shows the Split Hopkinson bar in the 'Advanced technology research center' (ATRC) Laboratory of Oklahoma State University (OSU). Figure 4.3 shows the schematic of the Hopkinson bar. The gas gun stores compressed air at variable pressures. The compressed air is available in the lab through a pipeline. The gas gun has valve to release the air into the barrel of the gun, which is supported by a bearing block.

Figure 4.2: Split Hopkinson pressure bar.

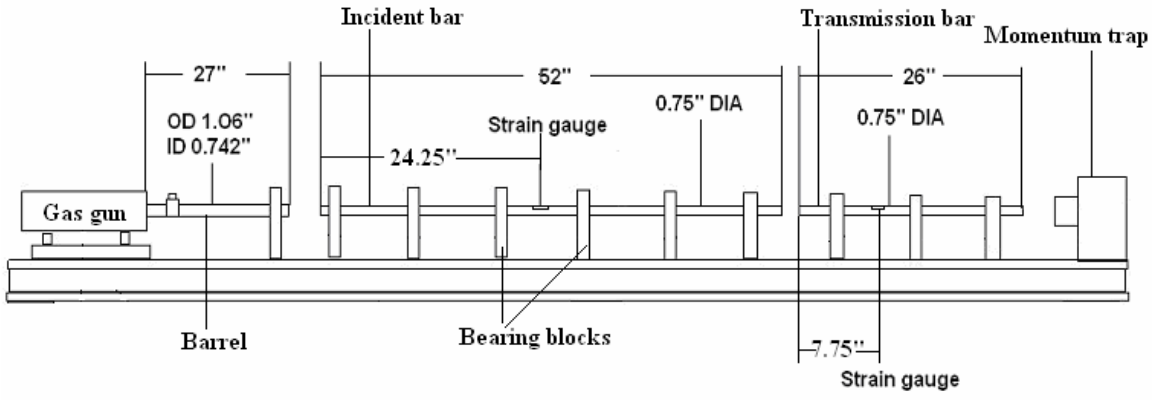

Figure 4.3: Schematic of the SHPB in the ATRC at OSU.

The striker bar is inserted in the barrel. The strikers used, had lengths of 4", 6" and 10", to vary the length of the pulse. All the striker bars, the incident bar and the transmission bar were made of Aluminum alloy7075-T651. Holes of diameter 3/8" were drilled across the length of the barrel to vent the air from behind the striker. Figure 4.4 shows the barrel with holes.

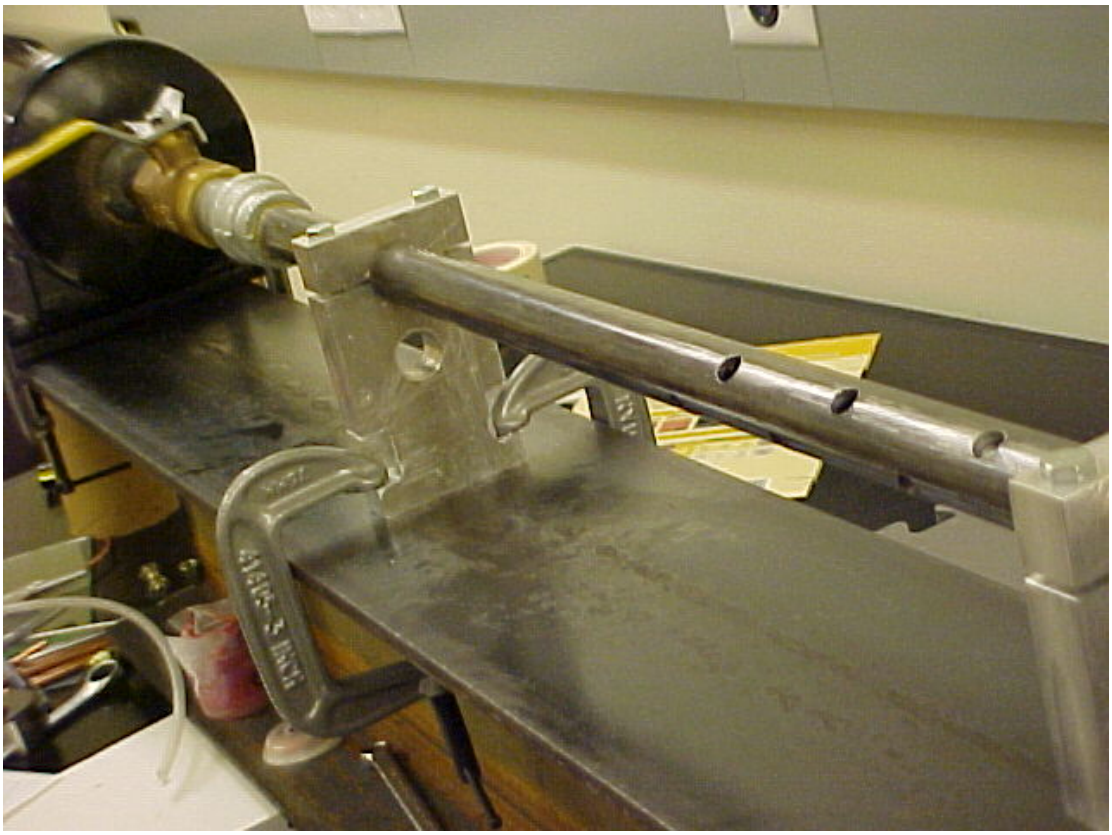

Figure 4.4: Barrel with holes.

4.3 Data acquisition

The physical quantity to be measured in this case is the strain in bars. This is accomplished by bonding strain gauges to the surface of the bars. In an ideal case one strain gauge on each bar is sufficient to measure the strain, but the problem of bar bending has to be dealt with, and hence a pair of strain gauges is used on both the bars. The strain gauges are at the same location along the bars and are exactly 180^{o} apart.

During bar bending both the gauges will measure the same strain but they will be opposite, meaning one will be in tension and the other will be in compression. Figure 4.5

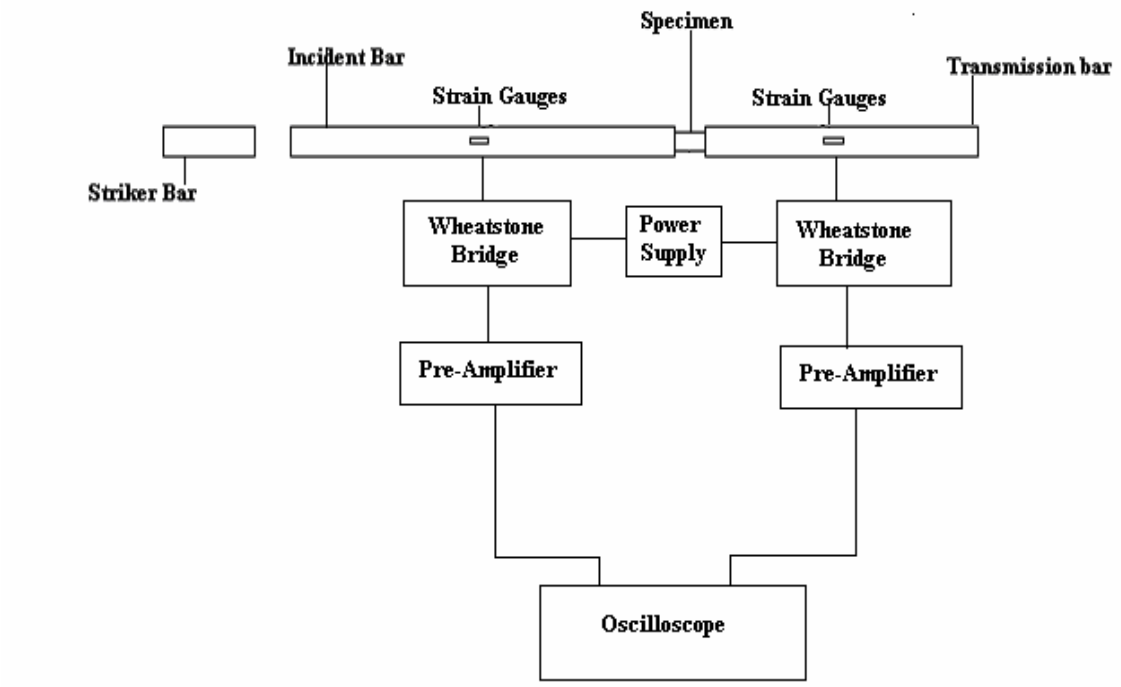

Figure 4.5: Schematic of the data acquisition system.

shows the schematic of the data acquisition system. The two strain gauges on each bar form the two arms of the respective Wheatstone bridges. The bridges are powered by a DC Power Supply (18V). The output is taken from the bridges to preamplifiers and subsequently to the oscilloscope.

4.4 The metallic resistance strain gauge

Figure 4.6 shows a typical foil strain gauge. The strain gauges used for the measurement had a resistance of 1000 ohms. Some of the characteristics [Engineering Data sheet for strain gauges, Measurements Group Inc.] of the strain gauges are as follows. The gauges are of open-faced construction with a 1mil tough, flexible polymide film backing.

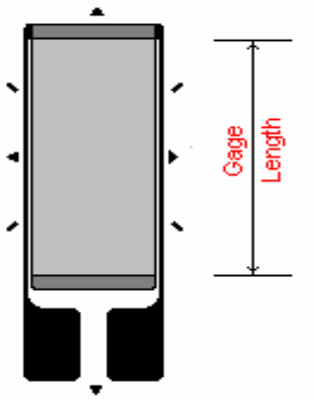

Figure 4.6: Typical foil-type single element strain gauge [24].

The gage factor is $2.080 \pm 0.5\%$ at 24^{o}C. If the bond between the strain gauge and the surface is sufficiently good then surface strains can be accurately measured by the strain gauge. The strain gauge is basically a resistance foil. If the length of the foil changes then the resistance also changes. The strain measured is directly proportional to the change in resistance which in turn is directly to the change in the gage length of the foil strain gauge. The fundamental formula for calculating the strain [25] is

$$\varepsilon = \frac{1}{F}\frac{\Delta R}{R} \qquad \text{(Eq 4.12)}$$

Where F is the gage factor of the strain gauge, ΔR is the change in resistance and R is the original resistance of the gauge.

4.5 Wheatstone bridge

Figure 4.7 shows a simple Wheatstone bridge. It comprises of 4 arms (resistors). It requires a supply voltage and gives a corresponding output. For the bridge shown below, the output of the bridge can be calculated as,

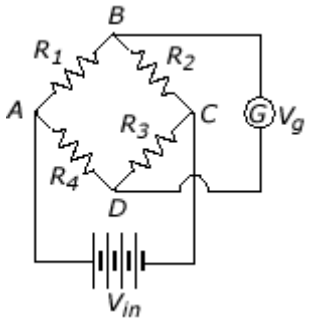

Figure 4.7: Wheatstone bridge [26].

$$Vg= \frac{R_1R_3 - R_2R_4}{(R_1 + R_2)(R_4R_3)} V_{in} \tag{4.13}$$

Initially the bridge is balanced and the output Vg is equal to 0. Hence equating equation (4.13) to 0, we have $R_1R_3 - R_2R_4 = 0$ and thus,

$$\frac{R_1}{R_3} = \frac{R_2}{R_4} \tag{4.14}$$

The above equation can be used to select the resistors.

In case of a change in the resistance of the resistors, we have the following relation,

$$Vg= \frac{(R_1 + \Delta R_1)(R_3 + \Delta R_3) - (R_2 + \Delta R_2)(R_4 + \Delta R_4)}{(R_1 + \Delta R_1 + R_2 + \Delta R_2)(R_4 + \Delta R_4 + R_3 + \Delta R_3)} V_{in} \tag{4.15}$$

A derivative of the Wheatstone bridge is the strain bridge. The arms of the bridge are replaced by strain gauges. Figure 4.8 shows a typical circuit for using strain gauges. A balance control is incorporated in the circuit so that the initial voltage can zeroed. The strain bridge that was used for the Hopkinson bar had four strain gauges on all four arms. This full bridge was used since the thermal characteristics of all the gauges are the same and hence good temperature compensation can be achieved. This circuit is shown in figure 4.9.

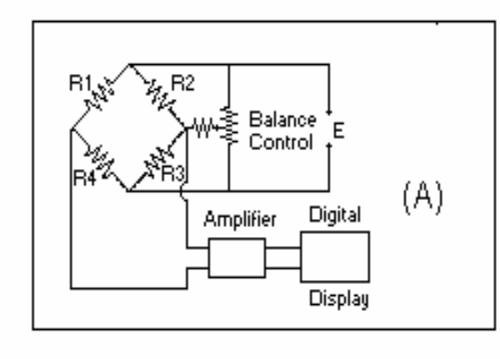

Figure 4.8: Typical Wheatstone bridge [24].

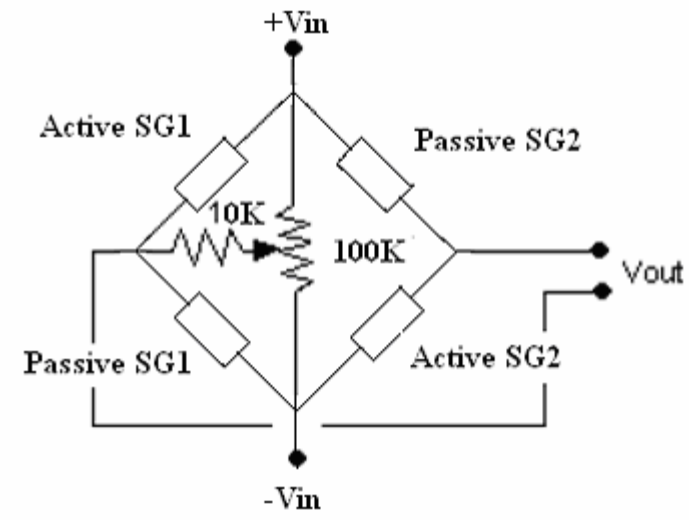

Figure 4.9: Wheatstone bridge for the current setup.

The bridge output was given to a preamplifier through P2220 passive probes. ADA400A (Tektronix) preamplifiers were used. The primary purpose was to convert the differential signal from the bridge to a coaxial one. The amplifier has a CMRR (Common mode rejection ratio) of 100,000 to 1 in the frequency range of DC to 10 KHz. Both the preamplifiers were powered by a Tektronix 1103 power supply. The coaxial output was given to a Tektronix TDS2014 oscilloscope.

4.6 Testing procedure

All the CSA samples were cut using a low speed diamond wheel cutter (MTI Corporation). The blades were made of silicon carbide and were 0.4mm thick. Samples of thicknesses 0.1" and 0.15" were cut and were later on polished on a fine grade silicon carbide paper. Figure 4.10 shows some of the samples used for testing.

Figure 4.10: CSA samples used for testing.

Pulse shapers made of copper110 and aluminum3003 were used to shape the incident pulse. The pulse shapers were cut from sheets and tubes. The aluminum sheets were annealed for 30 minutes at a temperature of 415°C whereas the copper sheets were annealed at a temperature of 425°C for 80 minutes. Once the shapers and the samples were ready, the striker bar was inserted inside the barrel. A small amount of grease was applied immediately before testing, on both the end faces of the incident and the transmission bars so as to keep the sample motionless due to gravity and to reduce friction. The pulse shapers were attached to the front end of the incident bar with grease. Then, the tank was filled with pressurized air. The offset voltage was nullified for each bridge using the potentiometers and the trigger was set on the oscilloscope. Finally the air inside the tank was released with help of a manual ball valve. A schematic of the pulse shaper is shown in figure 4.11

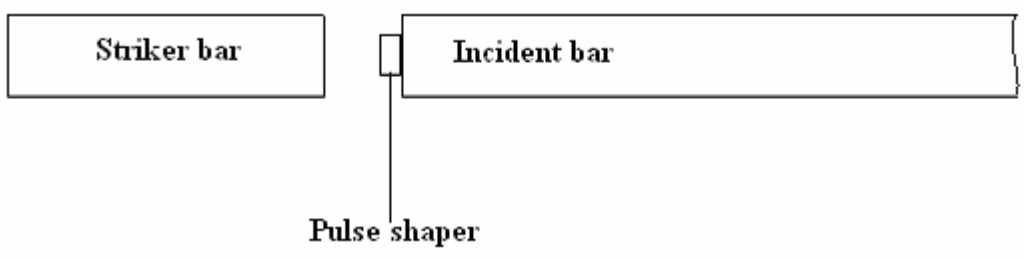

Figure 4.11: Schematic of a pulse shaper.

4.7 Preliminary tests

1. Alignment check for incident bar: In this test the two bars (incident and transmission) are held apart and the incident bar is struck with the striker bar without any shaper. After impact, a compression pulse of

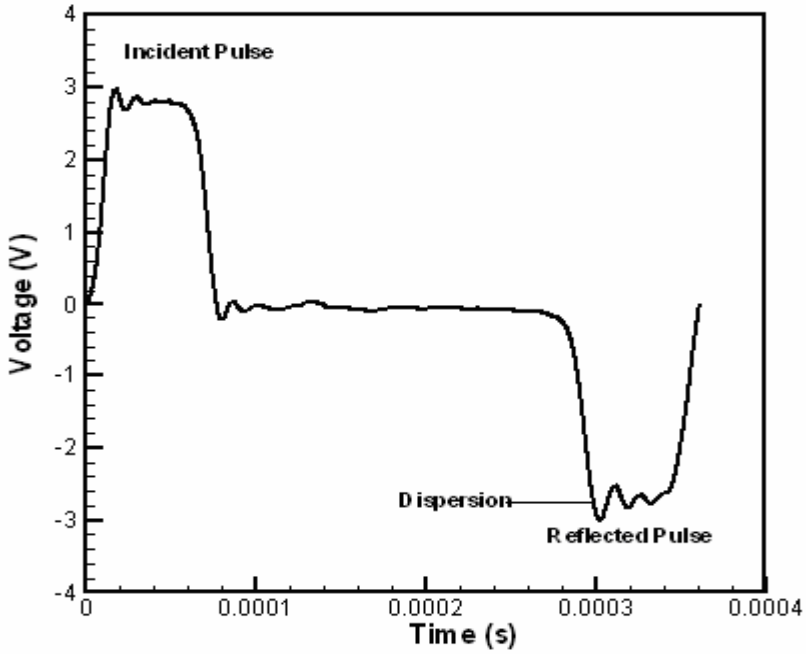

Figure 4.12: Alignment check for incident bar.

certain magnitude travels along the axis of the bar and since the other end is not constrained, the pulse is reflected back as a tensile wave of the same magnitude. Figure 4.12 shows the results of this test. As shown in the figure, the incident and the reflected

pulse are same in magnitude. One important feature of the stress wave propagation in thin bars is dispersion. Dispersion is the small variation in the magnitude of the waves due to 1-D stress status and/or lateral inertia effects. The waves traveling along the bars have a wide bandwidth of frequencies. It can be seen from the above two figures that the waves are trapezoidal in nature. For a trapezoidal wave, the dispersion effects are reduced because of the increased rise time. The time can be increased by using pulse shapers.

2. Alignment check for transmission bar:

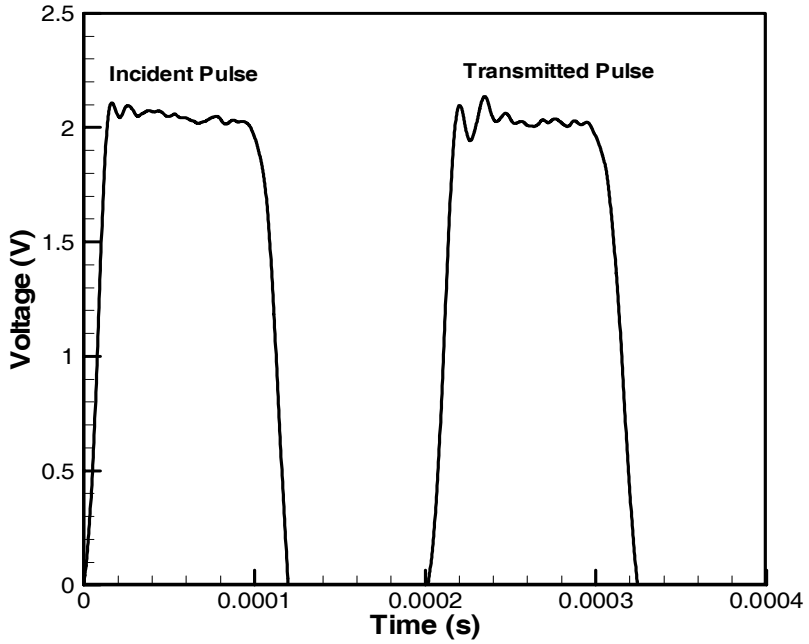

Figure 4.13: Alignment check for transmission bar.

In this test the incident and the transmission bars are held together with a thin layer of grease, and the front end of the incident bar is impacted with the striker bar.

In this case the compression wave passes through the incident bar into the transmission bar unaltered due to the same impedance of the two bars. From the above figure, the pulses are of the same magnitude and width, while dispersion still remains an issue.

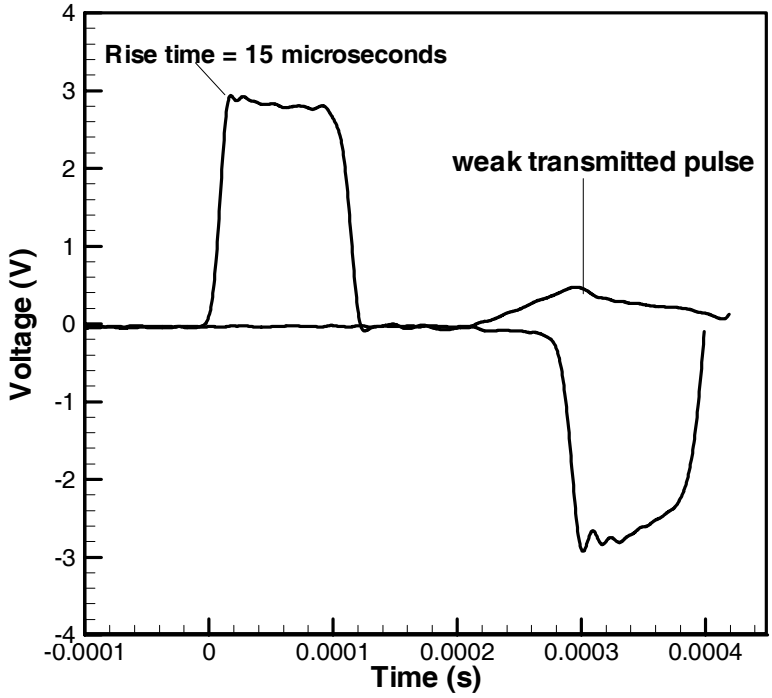

Figure 4.14: Weak transmitted pulse.

Figure 4.14 shows the results for a test conducted on a CSA sample of thickness 0.08" and diameter 0.65". Apparently, the transmitted signal is very small and is about five times smaller than the incident pulse since a major part of the incident pulse is reflected back. CSA has low impedance and hence the transmitted signal is very weak. This may lead to improper interpretation of the results since the signal to noise ratio is small. From equation (4.11) it can be concluded that for constant stress in the material, the transmitted strain can be increased by using a material that has a lower Young's modulus (E) and/or reducing the area ratio A/A_s. Chen et al [27] accomplished this by substituting a hollow Aluminum alloy bar. The hollow bar reduced the area ratio A/A_s, and as a result the transmitted signal was mechanically amplified.

The transmission bar for the SHPB in the current study, as shown in figure 4.15, is a hollow bar made of aluminum alloy 6061. The bar has an outer diameter of 0.75" and an inner diameter of 0.645". An end cap made of aluminum alloy

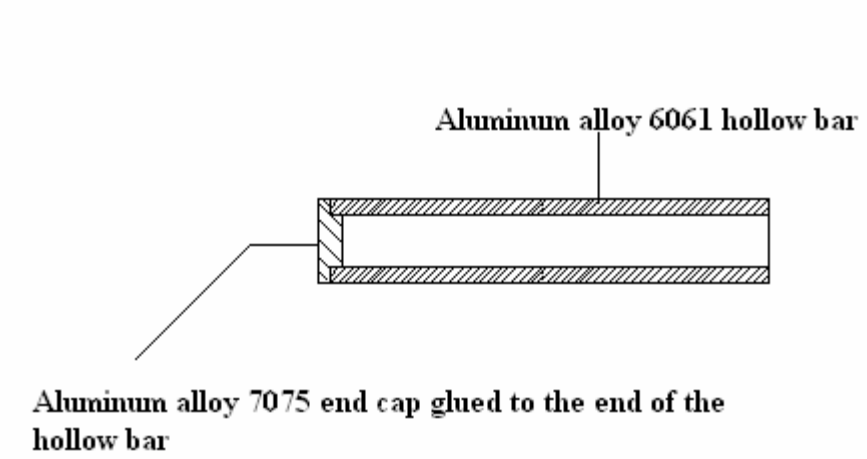

Figure 4.15: Longitudinal cross-section of the hollow transmission bar.

7075 was glued to the impact end of the hollow transmission bar to support the specimen. The thickness of the cap was maintained as small as possible (~1mm) to reduce the effects due to impedance mismatch of the two aluminum alloys. Figure 4.16 shows that the transmitted signal was increased by 5.6 times. Accordingly, the formula for calculating the strain in the specimen [27] was modified to

$$\varepsilon = \frac{c}{L}\left[(1 - A_r)\int_0^t \varepsilon_i(t)dt - (1 + A_r)\int_0^t \varepsilon_r(t)dt \right] \qquad (4.18)$$

From figure 4.14 the rise time for the incident pulse is about 15 microseconds. With such small rise time, when the incident pulse reaches the bar-specimen interface, it may plastically deform the low impedance material at that end and since the wave speed is low, the other end of the specimen will have smaller strains.

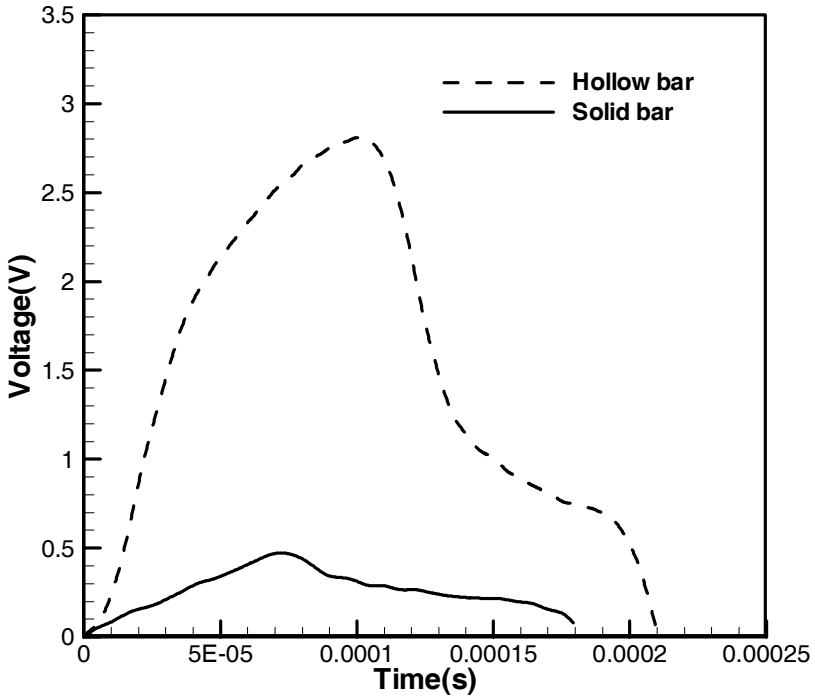

Figure 4.16: Mechanical amplification of the transmitted signal.

As a result, equilibrium cannot be achieved due to non-homogenous deformation in the specimen. To reach equilibrium the wave has to travel back and forth in the specimen for exactly π (3.14) number of times [28]. Therefore, by loading the specimen with a slowly rising incident pulse, the deformation in the specimen will be gradual and stress equilibrium can be reached. As mentioned in Chapter 2, the rise time can be increased by using pulse shapers and to this effect pulse shapers (disks) made of annealed copper and aluminum were used.

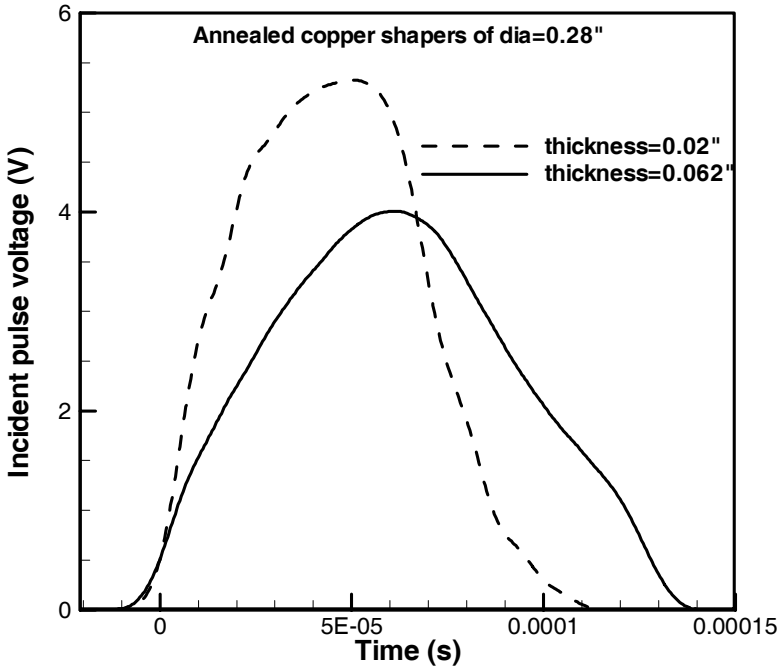

Figure 4.17: Effect of thickness of copper pulse shapers on the incident pulse.

Figures 4.17-4.20 show the effect of various pulse shapers on the incident pulse at a constant pressure of 20 psi. On being impacted by the striker bar, the pulse shaper deforms plastically and spreads the wave. If a pulse shaper is used, the load is gradually transferred to the incident bar. Figure 4.17 shows the effect of the thickness of the copper pulse shapers of the same diameter. With the increase in thickness, the width of the pulse and subsequently the rise time of the incident pulse increases. By using a copper pulse shaper of thickness 0.062" a rise time of 70 microseconds was achieved, but it was not sufficient to achieve equilibrium. From figure 4.18 it can be seen that the width of the pulse increases when the diameter of the shaper is reduced.

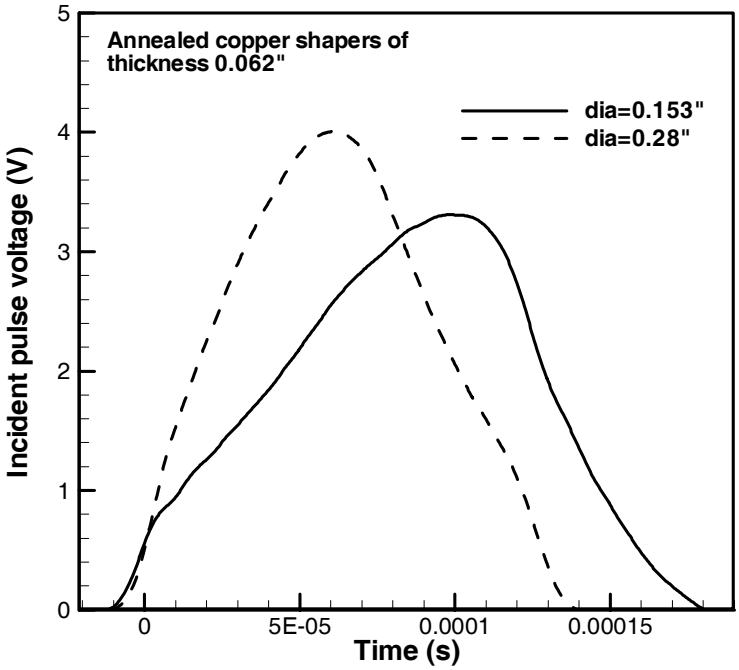

Figure 4.18: Effect of diameter of copper pulse shapers on the incident pulse.

Figure 4.19 depicts a significant increase in the rise time and the width of the pulse with increasing thickness of the aluminum shapers. The best shape (figure 4.19) was obtained by using an aluminum shaper of diameter 0.28" and a thickness of 0.09". Figure 4.20 shows the effect of the diameter of the aluminum shapers on the incident pulse. It can be seen that the rise time and the width achieved by using a shaper diameter of 0.153" are more than those achieved by using a shaper diameter of 0.28" for a constant thickness of 0.09". The aluminum pulse shaper of diameter 0.28" generates a pulse that has a decreasing slope, so after an initial small period of loading, the pulse has a tendency to flatten, thereby reducing the loading rate. Such a pulse is more likely to create equilibrium conditions and hence this shape was preferred.

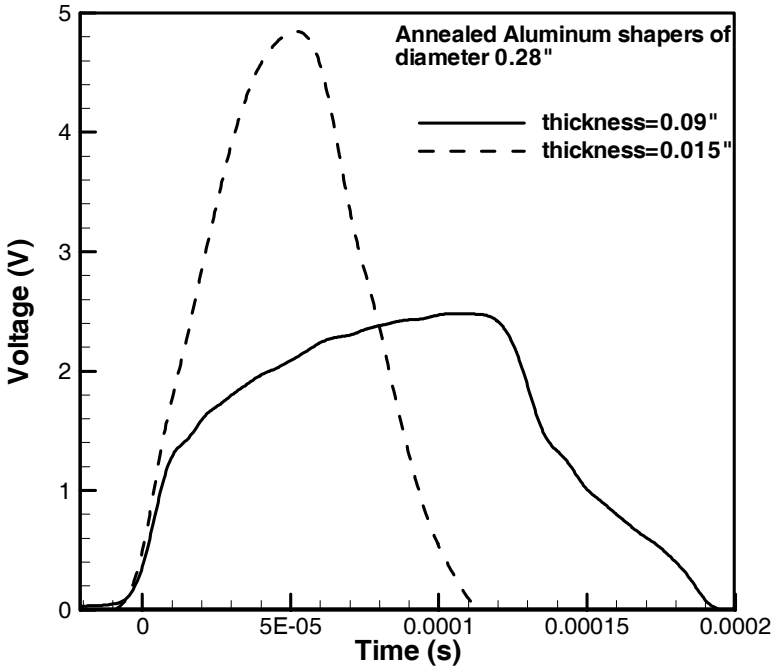

Figure 4.19: Effect of thickness of aluminum pulse shapers on the incident pulse.

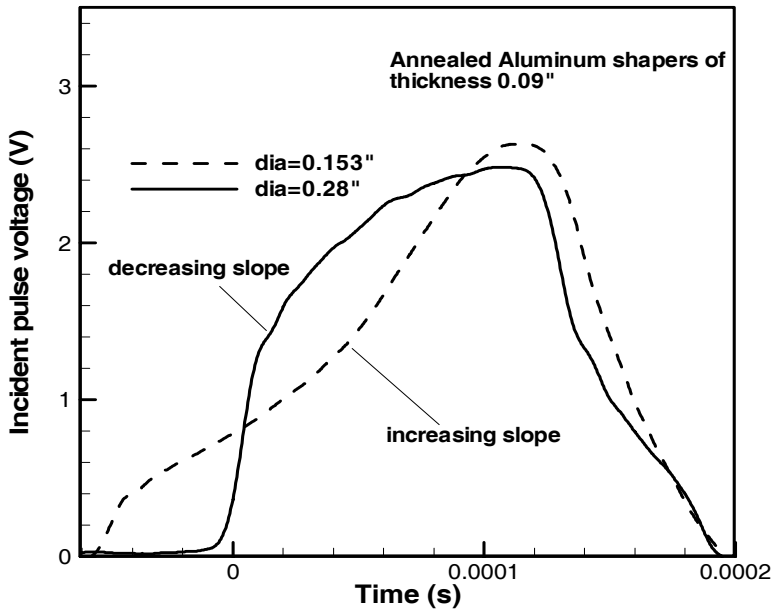

Figure 4.20: Effect of diameter of aluminum pulse shapers on the incident pulse.

Before getting to this shaper various pulse shapers were tested. Copper and aluminum shapers of thicknesses 0.045", 0.026" and 0.042" and diameters 0.246" 0.216" 0.185" and 0.123" were used. Shapers in the form of rings and concentric rings were also tried, but the best results were obtained by maintaining the tank pressure to 20psi and using annealed aluminum shapers of diameter 0.28" and thickness 0.09". Figure 4.21 shows some deformed shapers that were used.

Figure 4.21: Deformed pulse shapers.

4.8 Results and discussion

Figure 4.23 shows the voltage signals for the SHPB test on CSA sample of thickness 0.1". The data obtained from the oscilloscope was very noisy (figure 4.22) and hence the data was smoothed in Tecplot software.

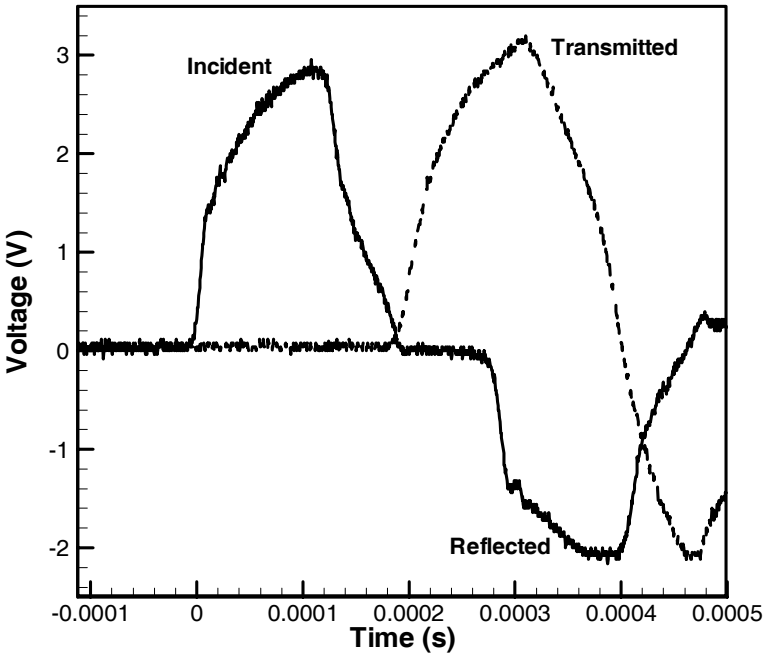

Figure 4.22: Raw voltage signals for SHPB test on CSA sample of thickness 0.1".

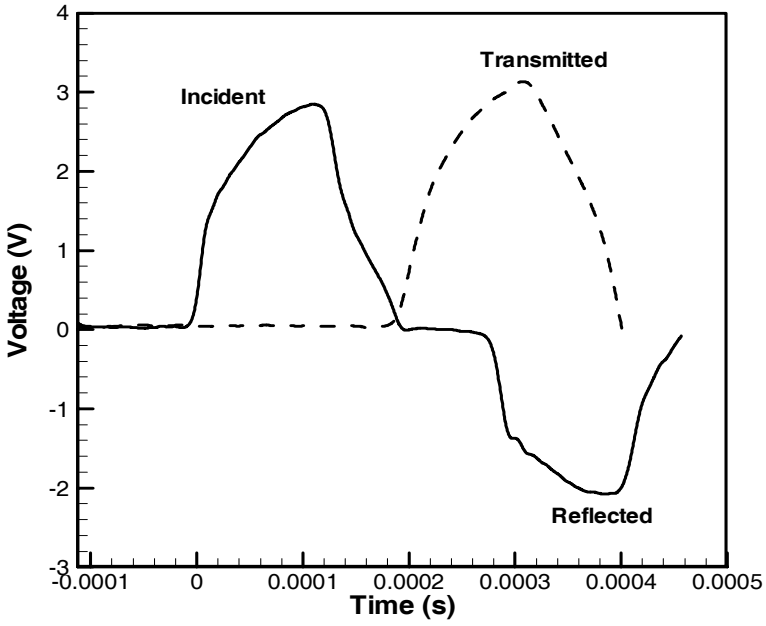

Figure 4.23: Smooth voltage signals for SHPB test on CSA sample of thickness 0.1".

Once this data was obtained, it was fed to a MATLAB program (Appendix) to check for the equilibrium and then calculate the stress and strain in the specimen.

Figure 4.24 shows the strains calculated from the voltage using the following formula

$$\varepsilon = \frac{2V_o}{GF * V_{in} * Gain} \tag{4.19}$$

whereVo is the output voltage, GF is the gain factor (2.02) for the strain gauges, Vin is the input voltage (18V DC) for the bridges and the Gain on the pre-amplifiers was set to 100. The strains thus obtained were processed using the formulas mentioned earlier in this chapter to obtain the strain rate and to check for equilibrium.

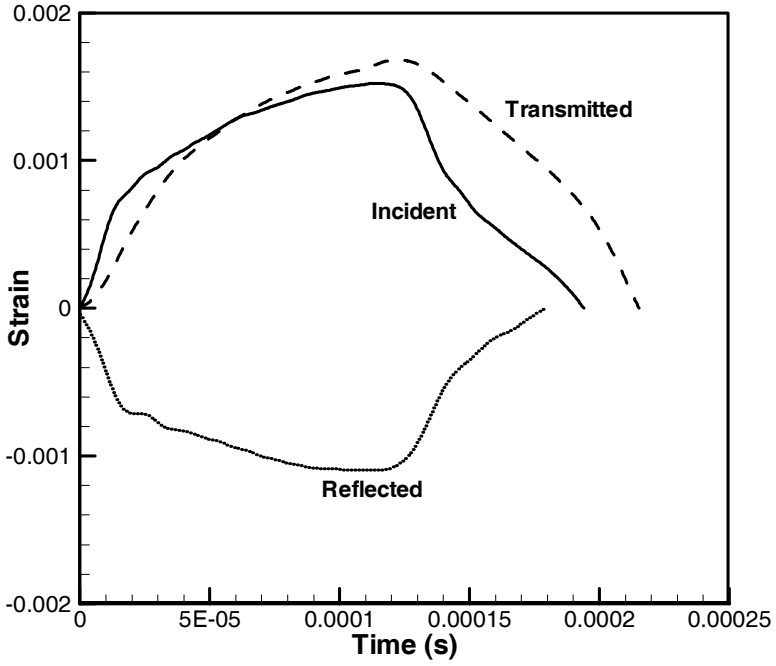

Figure 4.24: Bar strains for SHPB test on CSA sample of thickness 0.1".

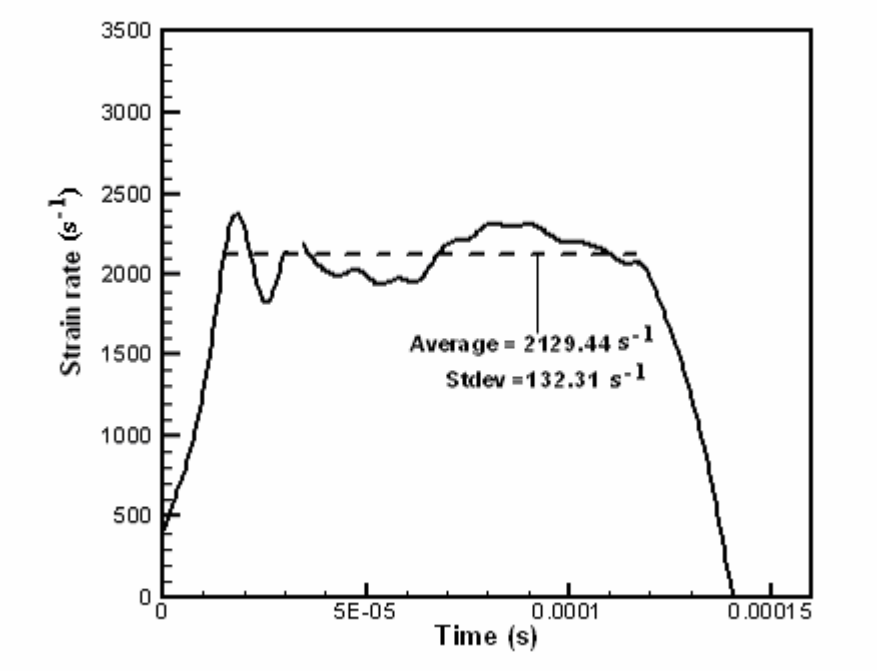

Figure 4.25: Strain rate for SHPB test on CSA sample of thickness 0.1".

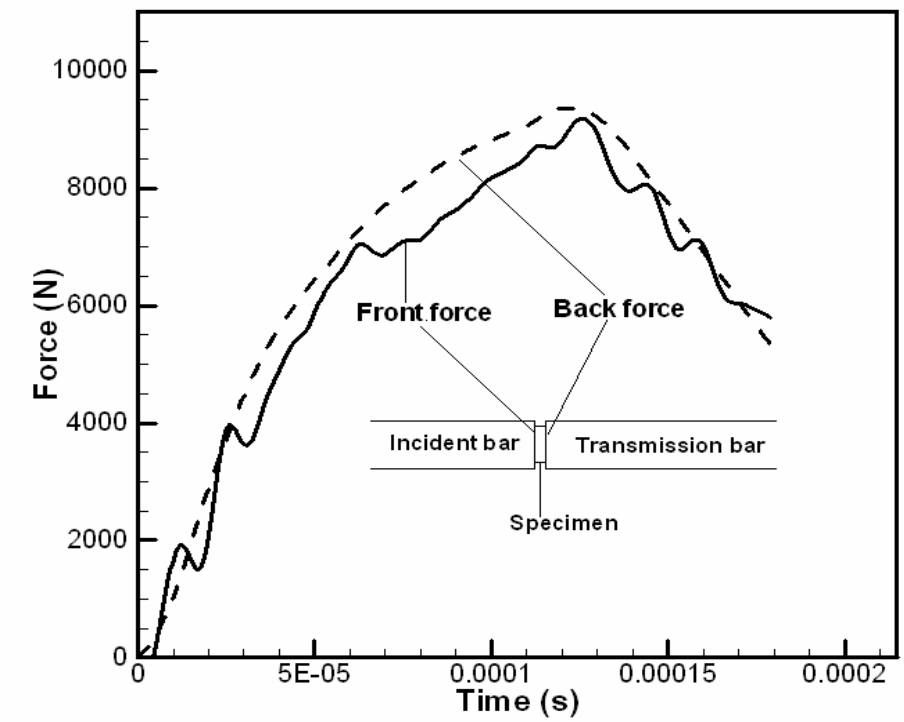

Figure 4.26: Equilibrium check for the SHPB test on CSA sample of thickness 0.1".

Figure 4.25 shows the strain rate for the SHPB test. It can be seen that the strain rate is not constant in the loading duration. It fluctuates from a value of $1990s^{-1}$ to $2378s^{-1}$. The average strain rate in this case was $2129.44s^{-1}$ with a standard deviation of 132.31. This is one of the best results obtained for all the tests conducted.

Figure 4.26 shows the comparison between the force on the right face of the incident bar (front force) and the one on the left face of the transmission bar (back force). The front force fluctuates with time and matches perfectly with the back force only at a few points. Figure 4.28 shows the stress strain curves for two samples of the same thickness (0.1”). An effort was made to maintain constant test parameters, but with the current setup it may be difficult to do so. The pressurized air in the tank was released with the help of a manual ball valve, so the speed at which the valve opened was different everytime and hence the striker speed was different. Hence the magnitude of the compressive stress wave traveling along the incident bar was different for different tests. It can be seen in the figure that curve having a higher strain rate is below the one having lower strain rate. The standard deviation for the average strain rate of $2537s^{-1}$ is $339s^{-1}$ (figure 4.27) where as the same for the average strain rate of $2129.44s^{-1}$ is $132.31s^{-1}$. So, the curve at the higher strain rate has a comparatively large fluctuation and hence is more unreliable. The strain rate was not constant during compression and hence the curves may not be perfectly valid. The average peak stress reached was ~ 42 MPa at a peak strain of 0.26. When higher striker speeds were used, the equilibrium was very poor. Since the strain rate was not constant, a well defined elastic region cannot be found in the curves.

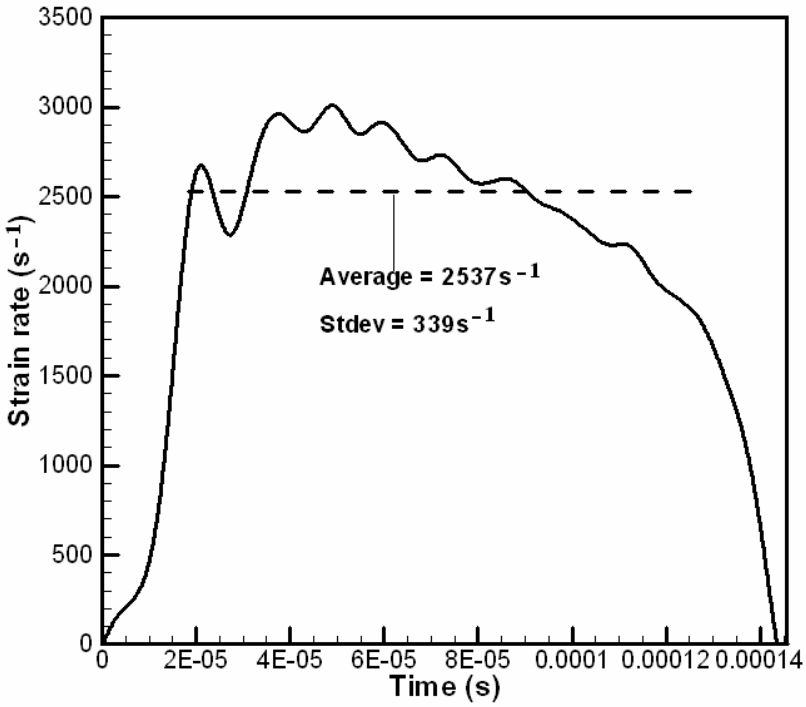

Figure 4.27: Strain rate for SHPB test on CSA sample of thickness 0.1" (sample 2).

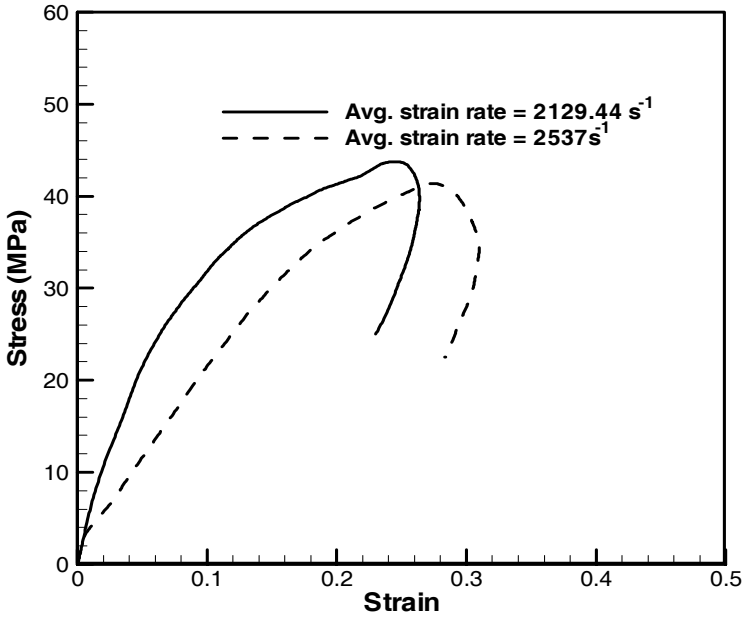

Figure 4.28: Stress-strain curves for the SHPB tests on CSA samples of thickness 0.1".

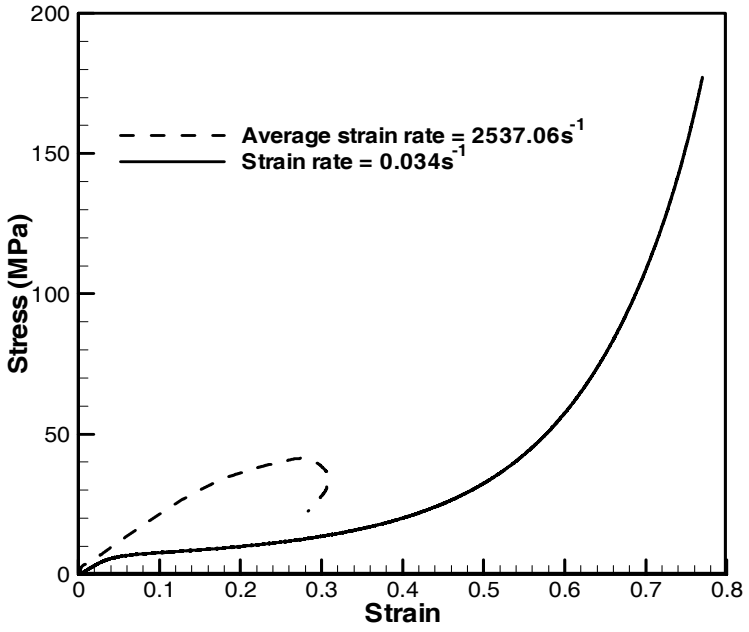

Figure 4.29: Comparison between the stress-strain curves for dynamic and quasi-static compression tests

Figure 4.29 shows the comparison between the stress-strain curves for dynamic and quasi-static experiments. A significant change in behavior can be seen. The CSA shows hardening behavior at an average strain rate of $2129s^{-1}$, and behaves much stiffer at this higher strain rate than at a lower strain rate.

Next, the sample length was increased from 0.1" to 0.15". It should be noted that with the increasing thickness, it is difficult to achieve equilibrium since the wave takes more time to travel back and forth inside the specimen. Figure 4.30 shows the incident, reflected and the transmitted strains for the SHPB test on CSA sample with thickness 0.15". Figure 4.31 shows the strain rate for the SHPB test on the 0.15" thick CSA sample. It can be

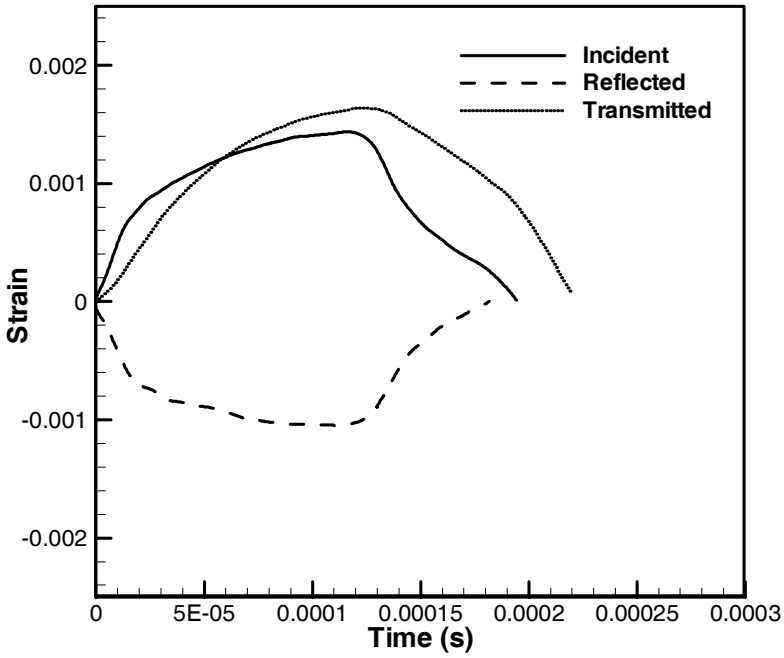

Figure 4.30: Bar strains for SHPB test on CSA sample of thickness 0.15".

seen that the strain rate again fluctuates during the loading period. In this case the strain rate varied from 1177.88s^{-1} to 1574.16s^{-1}, with an average value of 1505.33s^{-1} and a standard deviation of 97s^{-1}. Figure 4.32 shows the comparison between the front force and the back force. It can be seen that the two curves separate after a small initial period. Figure 4.33 shows the stress strain curve for the test. Again, this curve does not have a well defined elastic part because of the non-constant strain rate during loading.

Considering all the issues, no comparison was made between the stress strain curves at the two strain rates as this would lead to incorrect conclusions.

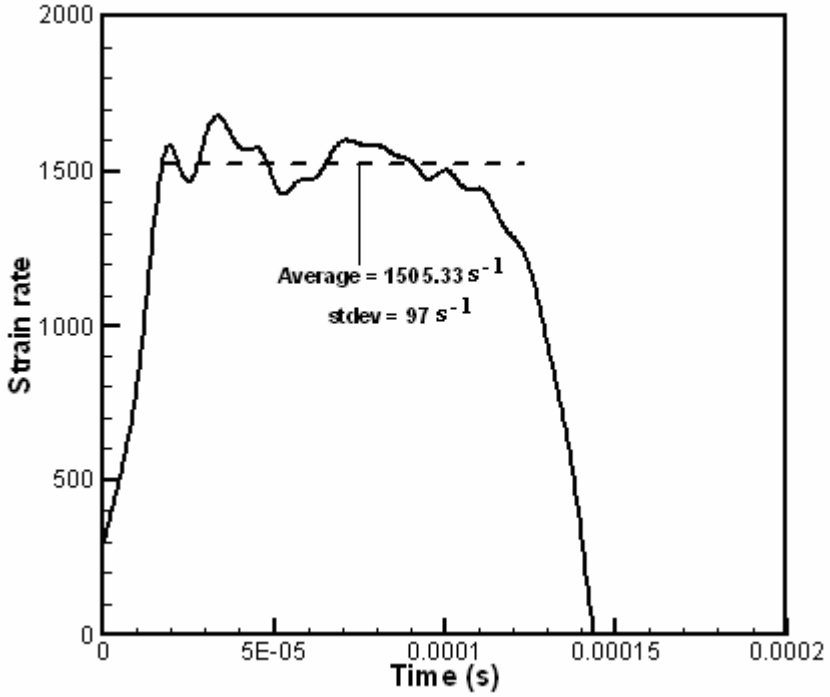

Figure 4.31: Strain rate for SHPB test on CSA sample of thickness 0.15".

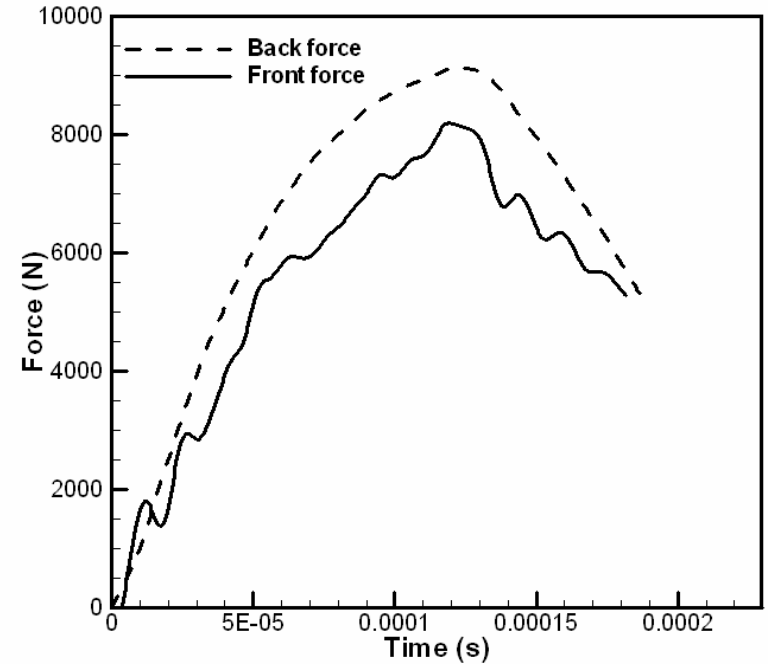

Figure 4.32: Equilibrium check for the SHPB test on CSA sample of thickness 0.15".

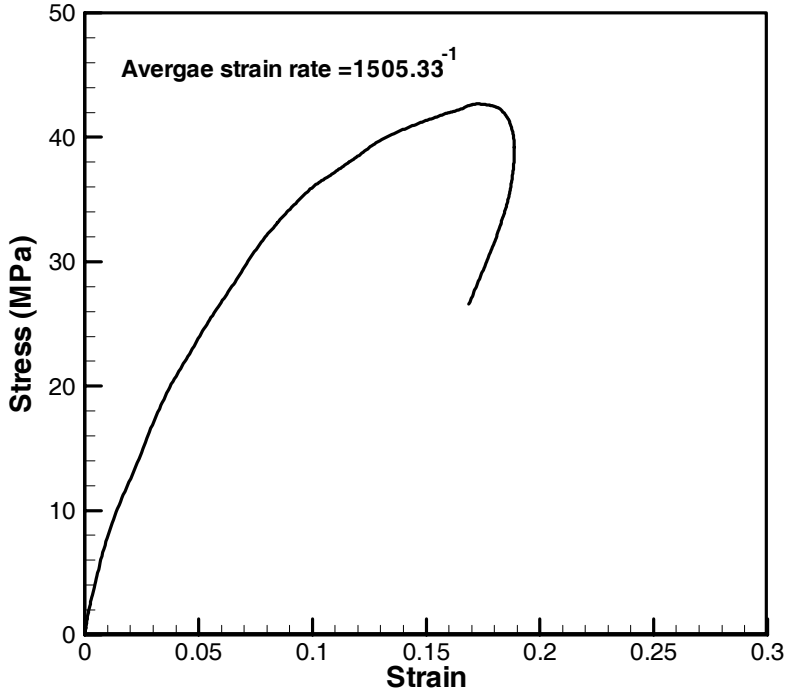

Figure 4.33: Stress-strain curve for the SHPB test on CSA sample of thickness 0.15".

The results can only be considered as an estimate of the material properties of CSA at high strain rates.

Some problems with the SHPB testing are mentioned below.

- Sample preparation: As mentioned previously, all the samples were cut using a diamond saw cutter. The thicknesses of these samples were found to be accurate within a range of 0.1-0.2mm. After cutting the samples, they were polished using a 400 grit silicon carbide paper. While polishing, the hand pressure on the samples was maintained as constant as possible across the diameter of the specimen. When the samples were held between the bars, very tiny gaps were observed. For the results presented above these gaps were the smallest. Cutting perfect samples is a major issue and they should be cut with a precision machine.

- Short incident bar: With the increase in the thickness of the pulse shaper, the width of the pulse also increases. Since the incident bar is relatively short (52”), if the width of the pulse is larger than the width of the incident pulses shown above, the incident and the reflected waves may overlap (figure 4.34) and this may lead to incorrect results.
- Non-uniform bar diameters: The solid incident bar had slight variation in the diameter. There was no facility for turning such a long bar on grinding machine. The internal diameter of the hollow transmission bar was not checked and again there was no facility for boring such a long bar.

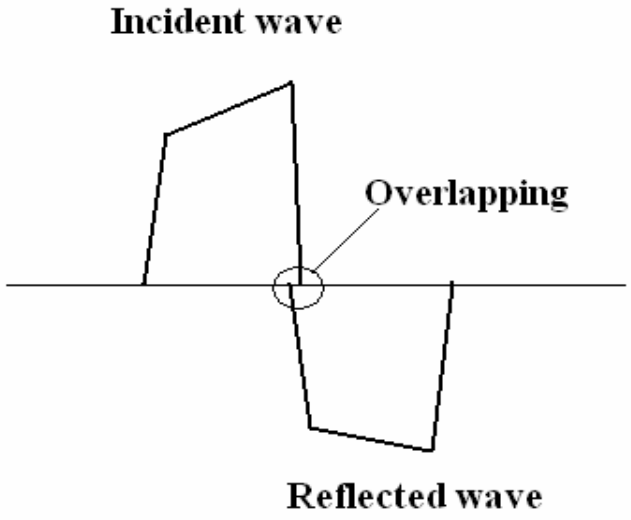

Figure 4.34: Overlapping waves due a short incident bar.

SHPB is a setup that requires care in various aspects such as alignment, signal conditioning and sample preparation. This setup originally had severe alignment issues and hence a thorough change has been made in this setup for experiments that lead to the results presented herein.

CHAPTER 5

NANOINDENTATION

5.1 Nanoindentation

All the nanoindentation tests were conducted using the "MTS Nano Indenter XP" system in the ATRC of Oklahoma State University. The system can reach a maximum indentation depth of 500 μm and a maximum load of 500 mN.

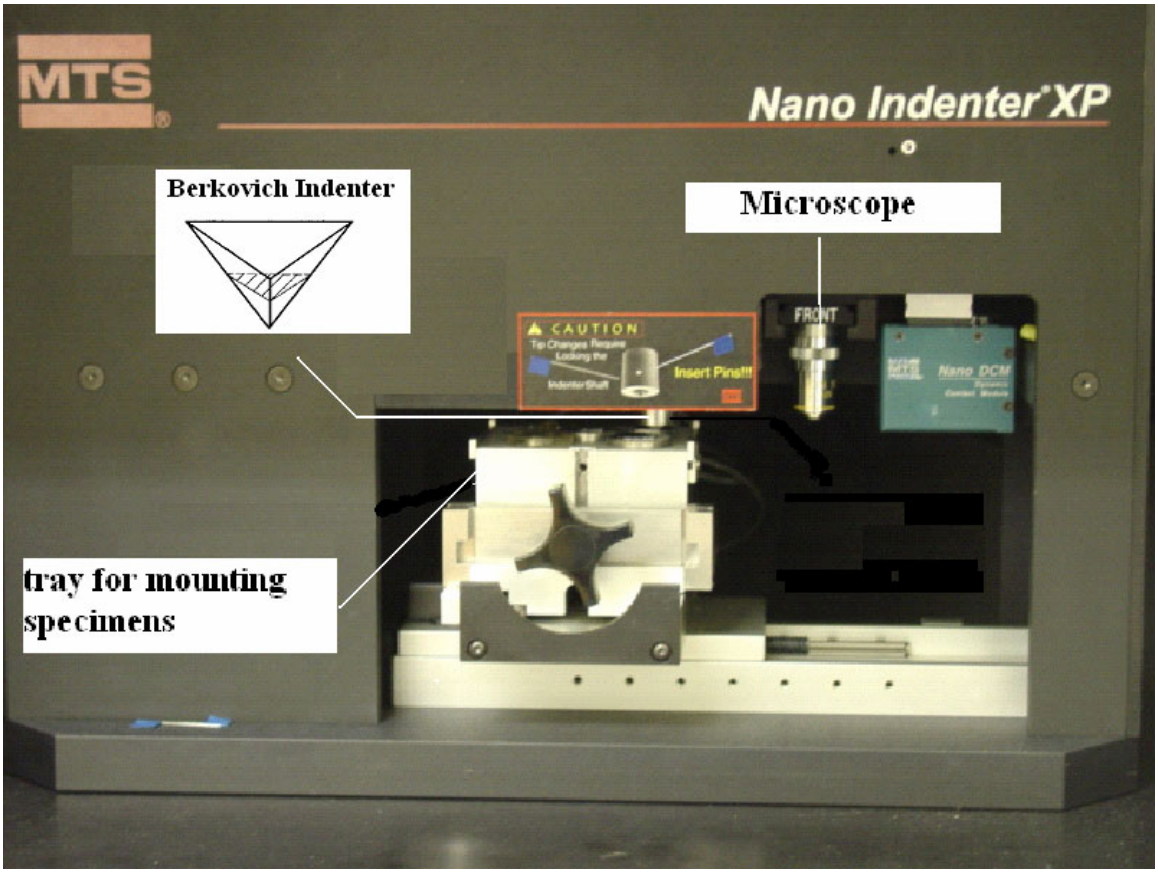

Figure 5.1: MTS nanoindenter.

The displacement resolution is 0.2 nm and the load resolution is 50 nN. The Berkovich indenter used is made of diamond. The geometry for the indenter is shown in Figure 5.2. The load and depth data is measured by using a software called Testworks. The movement of the nanoindenter can be controlled using the software. The Berkovich indenter has a three-faced pyramidal tip. The relation between the contact area *A* (in nm2) and the indentation depth, *h* (in nm), can be described as a polynomial function.

$$A = 24.37h^2 + 197.0h - 675.3h^{0.5} \quad (5.1)$$

The Berkovich indenter has a tip radius of 2.5nm and is modeled as a cone having an axisymmetric cone angle of 70.3°, hence the angle α in figure 5.2 is 19.7°.

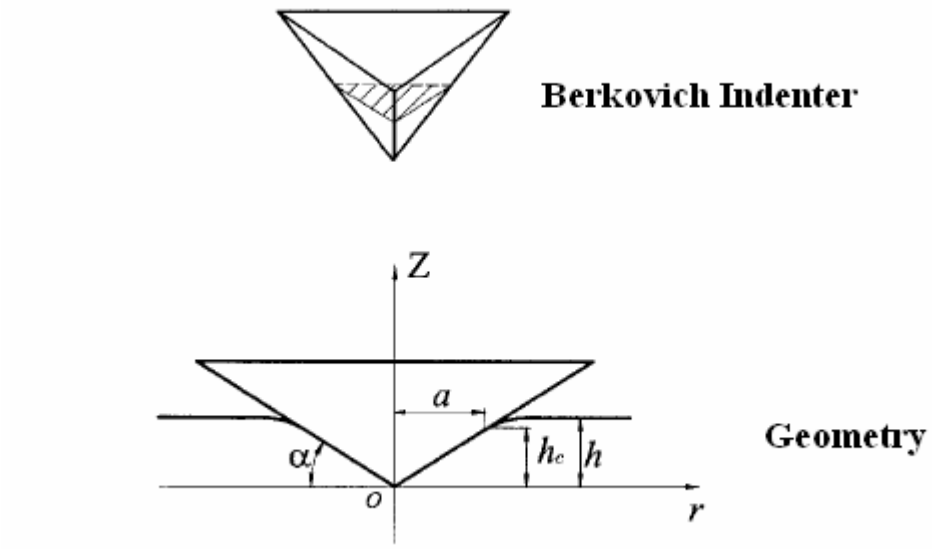

Figure 5.2: Geometry of the Berkovich Indenter [3].

Load-depth curves were obtained for a total of 3 specimens of different densities. Table 5.1 shows the densities of all the three CSA samples.

Table 5.1: Densities of CSA samples.

Sample	Density (g/cc)

Rectangular c/s sample 1	0.74
Cylindrical sample	0.48
Rectangular sample 2	0.53

The tray shown in figure 5.1 has holes for mounting cylindrical pieces. The specimens were glued to the top surface of these cylindrical pieces after they were leveled. Then the tray was mounted on the machine. Initially, after the indenter was changed to the Berkovich indenter, the tip was calibrated. During calibration, a spot on the top surface is chosen using the microscope inside the nanoindentation machine. After that the machine moves the sample tray to the indenter location and makes five indents on the spot chosen by the user on the sample surface. Four of the dents are at the four corners of a square and the last one is at the center. The indent at the center is selected by the user and that ends the calibration process. For any sample surface, a grid of points is specified so that the indentation can be done at these specified points. Other parameters such as allowable drift rate, surface approach velocity, surface approach distance etc are specified. All nanoindentation tests were performed in the air at room temperature (21^{o}C). After the indenter tip had made contact with the specimen surface, controlled indentation load was applied at the rate of 0.012mN/s, and the indentation load and indentation depth were recorded simultaneously using Testworks. The maximum indentation load for all the experiments was 2mN.Once load reached a value of 2mN, all the samples were unloaded. CSA is a viscoelastic material, as it was discussed in chapter 3. Because the rate of loading is slow and during indentation the contact area between the indenter and the material changes with time, this is a quasi-static boundary value problem with moving boundary between the indenter and the half space (material).Lu et al [3] obtained the

following equations by using the technique used by Radok [23] for solving the above moving boundary value problem for a linearly viscoelstic material.

$$h^2(t) = \frac{\pi(1-\upsilon)\tan\alpha}{4}\int_0^t J(t-\xi)\left[\frac{dP(\xi)}{d\xi}\right]d\xi \tag{5.2}$$

where h is the depth of indentation, α is the effective cone angle of the axisymmetric cone substituted for the Berkovich indenter, J is the creep compliance in shear. By substituting $\upsilon_0 t$ H(t) for P(t) in equation (5.2), where υ_0 is the constant loading rate and H(t) is the Heaviside unit step function, one gets,

$$h^2(t) = \frac{\pi(1-\upsilon)\upsilon_0\tan\alpha}{4}\int_0^t J(t-\xi)d\xi \tag{5.3}$$

For a constant loading rate, the differentiation of equation (5.3) yields,

$$J(t) = \frac{8h}{\pi(1-\nu)\tan\alpha}\frac{dh}{dP} \tag{5.4}$$

Equation (5.4) can be used to calculate the creep compliance, but as the experimental data can be scattered, the calculation of the derivative may induce some errors and hence Lu et al [3] proposed another method by substituting the following equation for generalized Kelvin model representation of the creep compliance in shear.

$$J(t) = J_0 + \sum_{i=1}^{N} J_i\left(1-e^{\frac{-t}{\tau_i}}\right) \tag{5.5}$$

where J_0 and J_i are the compliance numbers, N is the number of terms in the prony series and τ_i are the retardation times.

The following equation is obtained by substituting $P(t)= \upsilon_0 t$ and equation (5.5) in equation (5.3).

$$h^2(t) = \frac{1}{4}\pi(1-\nu)\tan\alpha\left[\left(J_0 + \sum_{i=1}^{N} J_i\right)P(t) - \sum_{i=1}^{N} J_i(\upsilon_0\tau_i)(1-e^{-(P(t))/(\upsilon_0\tau_i)})\right] \quad (5.6)$$

where h is the depth of indentation, α is the effective cone angle of the axisymmetric cone substituted for the Berkovich indenter, P is the indentation load and υ_0 is the loading rate.

Once the load-depth curves were obtained, the data was analyzed by using a software called "Creep calculator" [3]. The software fits the load-depth data in equation (5.6) and calculates the prony series parameters and then uses these parameters in equation (5.5) to generate the creep function Vs time curve.

5.2 Nanoindentation results

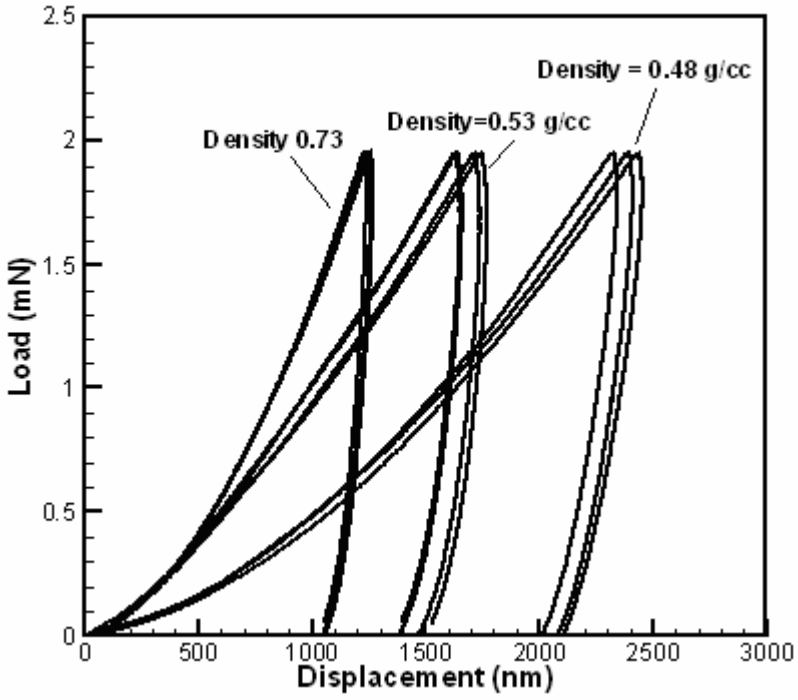

Figure 5.3: Nanoindentation load-depth curves for CSA samples of various densities.

As mentioned previously, the nanoindentation tests were conducted on CSA samples of three different densities. Figure 5.3 shows the load displacement curves for all the three samples at multiple locations. All the samples were loaded till a load of 2mN was reached and then they were unloaded. The average indentation depth at 2mN for the sample with density 0.73g/cc (four locations at the four corners of a square of side 40μm apart) was 1239.23 nm, for the one with density 0.53g/cc (four locations at the four corners of a square of side 40μm apart) was 1660.33nm and for the one with density 0.48g/cc (three locations 40μm apart) was 2453.86nm. The stiffness goes on increasing with the density and results are repeatable for every sample. This shows that the material is homogeneous to a reasonable extent. The average permanent depth of indentation after load recovery for the sample with density 0.73g/cc was 1032.85 nm, for the one with density 0.53g/cc was 1388.81nm and for the one with density 0.48g/cc was 2123.42nm.

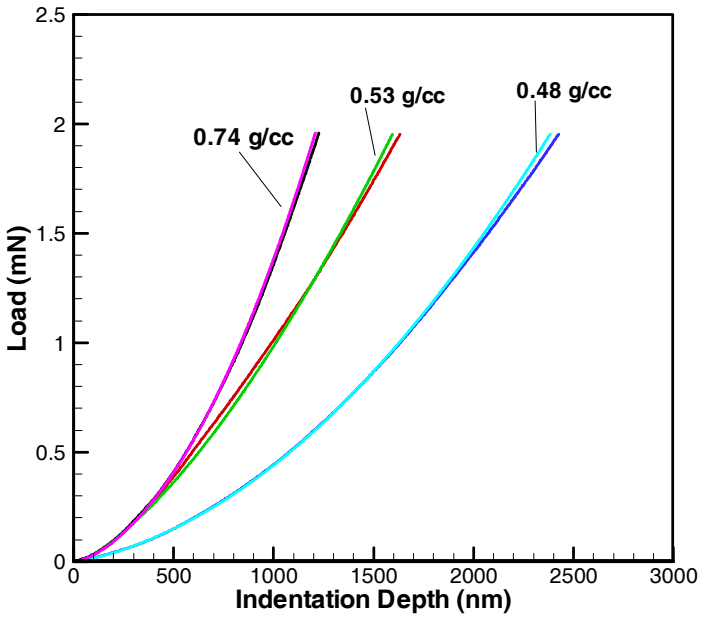

Figure 5.4: Experimental and curve fit data for nanoindentation on CSA samples.

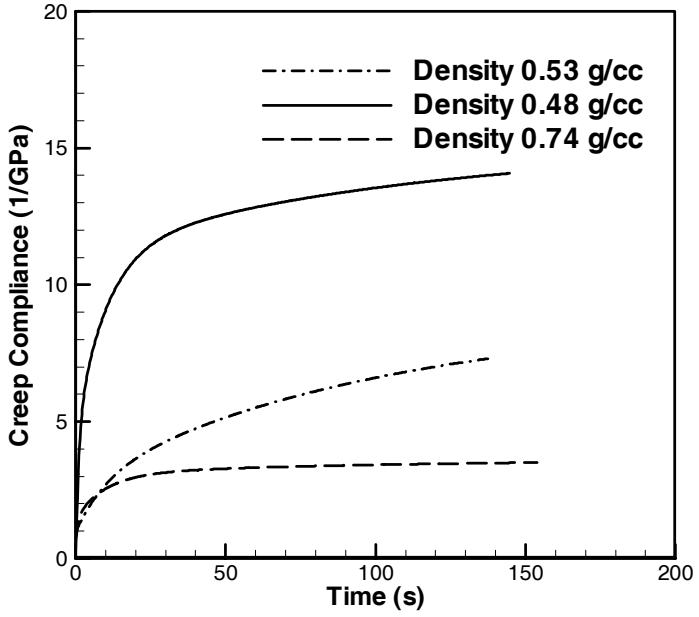

Figure 5.5: Nanoindentation creep compliance curves for CSA samples of various densities.

The test for every sample was carried out at an average of four different locations and the results were consistent. Figure 5.4 shows the comparison between the experimental and curve fit load-depth data for nanoindentation on three samples of different densities. The curve was fitted using equation (5.6). The prony series parameters calculated by fitting the data were used in equation (5.5) to get the creep compliance curves for the CSA samples as shown in figure 5.5. Table 5.2 shows the compliance numbers of the prony series obtained for the creep compliance curve.

Table 5.2: Prony series parameters for CSA samples with various densities.

i	Density=0.74g/cc	Density=0.53g/cc	Density=0.48g/cc
	J_i (1/GPa)	J_i (1/GPa)	J_i (1/GPa)
0	0.657112	0.959969	4.4157×10^{-9}
1	0.832075	5.1848×10^{-11}	4.453220
2	1.590449	1.8420840	6.632474
3	0.533182	5.956565	3.527571

4	0.044465	0.383860	1.554429
5	0.004358	0.033467	0.178648
6	0.000560	0.003509	0.018379
7	0.000182	0.000576	0.002108
8	0.000145	0.000283	0.000479

The retardation times τ_i entered in the software were 10^0 s, 10^1s, 10^2s, 10^3s, 10^4s, 10^5s, 10^6s and 10^7s.The creep compliance in shear and the shear relaxation modulus have the following relation.

$$\int_0^t J(t-\xi)\mu(\xi)d\xi = t \tag{5.7}$$

where μ is the shear relaxation modulus.

The Young's relaxation modulus can be obtained from the following relation

$$E(t) = 2(1+\nu)(\mu(t)) \tag{5.7}$$

where ν is the poisson's ratio.

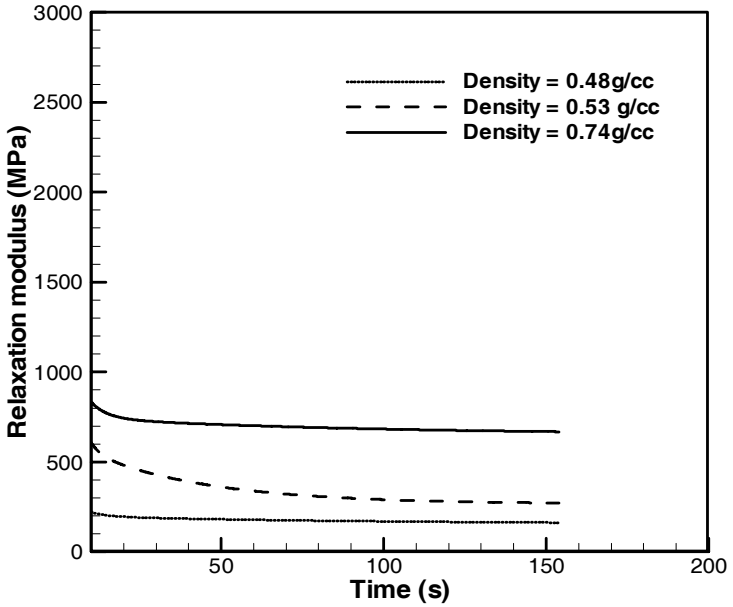

Figure 5.6: Relaxation modulus for CSA samples of various densities.

Since time dependant data was not available for the poisson's ratio, it was assumed constant (0.18).

Figure (5.6) shows the Young's modulus as a function of time. The data at the beginning when the indenter tip touches the material surface are not correct and hence were clipped to obtain the curves shown in the figure.

The results are summarized in table 5.3.

Table 5.3: Relaxation modulus at the end of 150s, for CSA samples of various densities.

CSA sample density (g/cc)	Relaxation Modulus (MPa)
0.74	669.1
0.53	272.6
0.48	163.6

It is interesting to note that the modulus goes on increasing with the density. Further, this data was compared with complex modulus at room temperature obtained from the DMA results and the values can be seen in figure 5.7.

Aerogels are known to exhibit a scaling behavior. The elastic modulus has the following power law relationship with the density.

$$E \propto \rho^{\alpha} \tag{5.8}$$

The data obtained from nanoindentation tests were used determine the value of the scaling exponent α by fitting a power law curve through the data points.

Figure 5.8 shows the power law fit for the data. The DMA tests were performed at a higher strain rate and hence the DMA data was not used in the calculation. It can be seen

from the figure that a good fit is not obtained since the data points are few. The value of the scaling exponent (α) obtained from the power fit is 3.11.

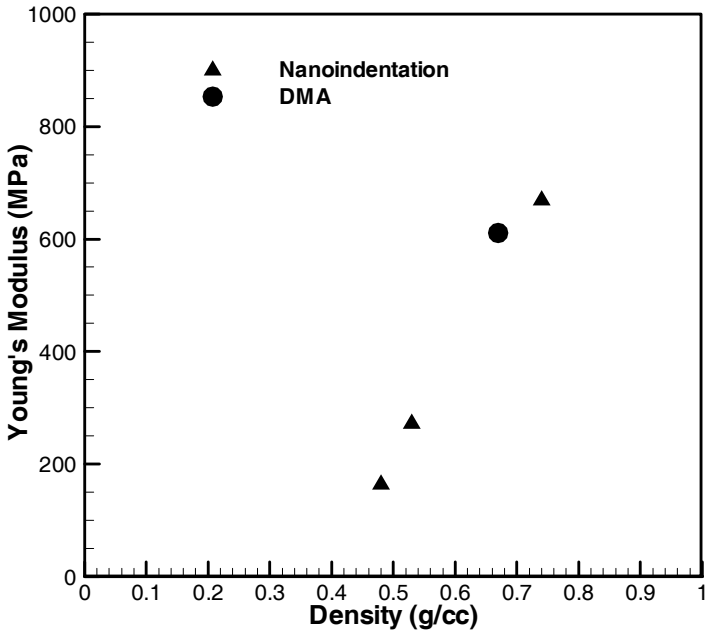

Figure 5.7: Variation of Young's modulus with density for CSA.

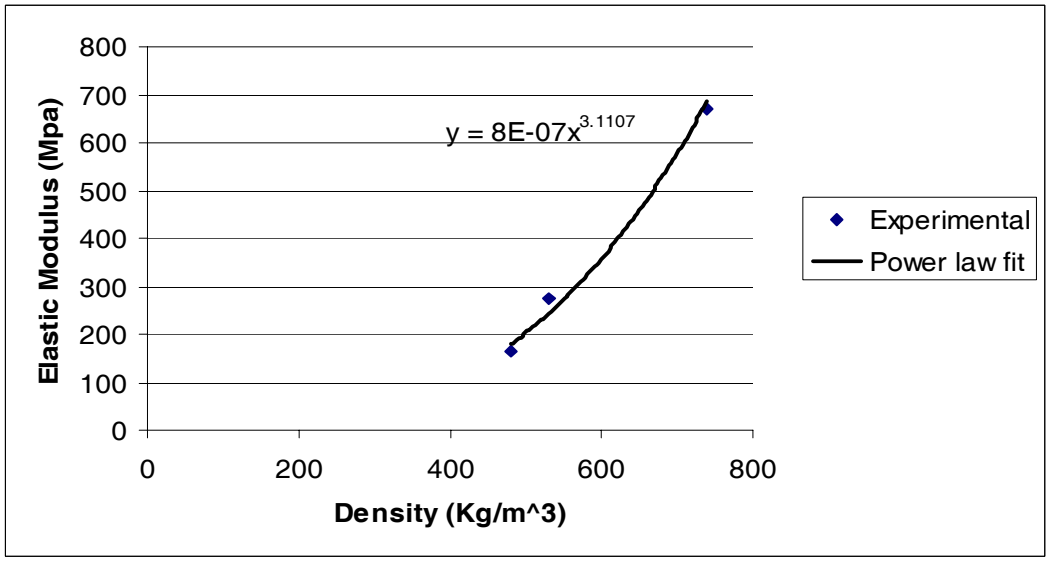

Figure 5.8: Scaling exponent for CSA based on nanoindentation tests.

CHAPTER 6

CONCLUSIONS AND FUTURE WORK

6.1 Conclusions

Aerogels manufactured by the sol gel process were strengthened by the addition of isocyanate crosslinker. The density of the crosslinked samples was found to vary from 0.48-0.74g/cc. The development of a new material opened the avenue for characterization through testing. With this opportunity, tests were conducted to characterize the material, namely nanoindentation, high strain rate testing using a split Hopkinson bar and dynamic mechanical analysis. The nanoindentation tests were conducted using a MTS Nano Indenter XP system. A Berkovich indenter was used for all the tests. Nanoindentation tests were performed on samples of densities 0.74, 0.48 and 0.53g/cc respectively and the load depth curves were obtained. From this data the creep compliance curves and subsequently the relaxation moduli were obtained. The load-depth curves indicate an increasing stiffness with the density. The Relaxation moduli data for the three samples at the end of 150s were fitted using a power law and the value of the scaling exponent determined was 3.11.

The split Hopkinson pressure bar was set up to conduct high strain rate testing on the CSA samples. A hollow transmission bar was used to increase the magnitude of the transmitted pulse since CSA has low impedance. Pulse shapers were used in an attempt to

achieve dynamic equilibrium. Perfect equilibrium and constant strain rate could not be obtained due to various problems. The results obtained can be considered as estimates of the material property of CSA. The stress strain curve for the average strain rate of 2129.44 s^{-1} was compared with the one at 0.034s^{-1}. The curve at higher strain rate shows different behavior, but again any sort of quantitative comparisons could not be made because of the issues involved.

The DMA tests were performed to determine the complex modulus in three point bending. A temperature scan was performed at temperatures ranging from -132 ^{o}C to 210 ^{o}C at a frequency of 1Hz. The storage modulus was found to decrease with increasing temperature. The storage modulus decreased by 95% from -132 ^{o}C to 210 ^{o}C. In the plot of tan delta, two peaks were observed, one at 130 ^{o}C, indicating the major glass transition and the other at -50 ^{o}C indicating the secondary transition. Next, a frequency scan was done at various temperatures. At all the temperatures, the modulus was found to increase with frequency. The curves at neighboring temperatures were shifted to obtain a master curve referred to 20 ^{o}C. Data for 25 decades was thus obtained.

6.2 Future work

Since crosslinked silica aerogel is a new material, a lot of work can be done to characterize it. Some additional work was done to characterize the thermo-mechanical behavior of this material, but successful results could not be obtained because of time and resource constraints.

A simple problem of uniaxial compression was modeled using the crushable foam model in the commercial FEM package, ABAQUS. Figure 6.1 explains the model geometry used in the simulation. CSA was modeled as a cylindrical sample having a diameter of

16mm and a length of 32mm. The CSA sample was held in-between two steel platens. Velocity loading was applied to the upper plate while the lower plate was constrained in all the directions. This was done to simulate the actual experimental conditions. Figure 6.2 shows the comparison experimental and simulation results. The crushable foam model in ABAQUS requires two important parameters, k (compression yield stress ratio) and k_t (hydrostatic yield stress ratio). These parameters were not available since there was no facility for conducting the volumetric compression test.

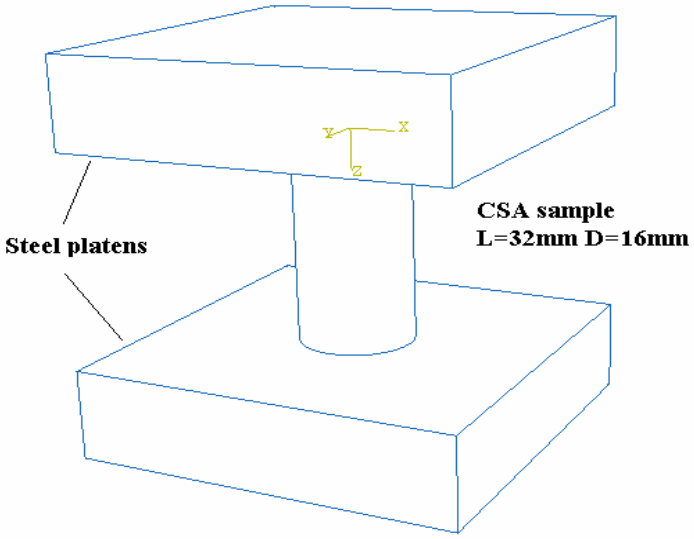

Figure 6.1: Model Geometry.

Hence the values were guessed and results obtained were in partial agreement with the experimental results. It can be seen that the results are in good agreement until a true stress value of 2500 psi and a true strain of 0.3. FEM was able to capture the early elastic behavior, but not the complete inelastic behavior. Hence volumetric testing needs to be carried out to obtain the required parameters in order to carry out the simulation.

Further, a numerical model can be constructed using neural networks. “Neural networks” is a powerful optimization tool and once the model is finalized, the values of the parameters in the model can be optimized using Neural Networks.

The validity of the master curve obtained from the DMA tests can be checked by conducting tests at lower frequencies.

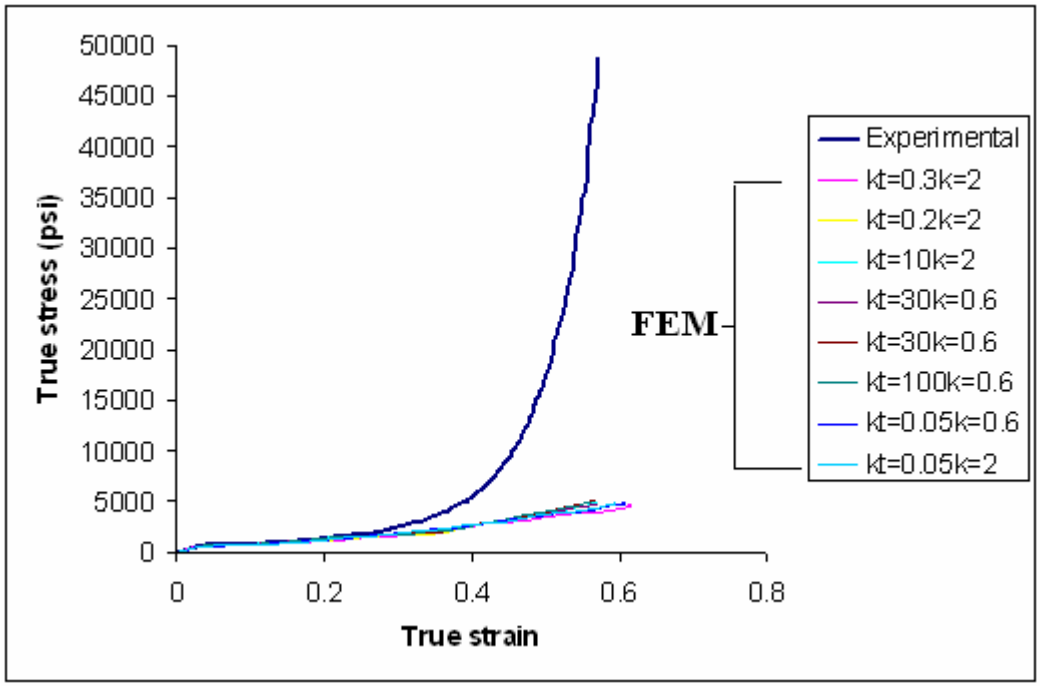

Figure 6.2: Comparison of experimental and FEM results for uniaxial compression on CSA.

REFERENCES

1. Leventis et al, "Nanoengineering strong Silica Aerogels", NanoLetters, 2002, Vol 2, No.9, 957-960

2. Menard K.P, "Dynamic Mechanical Analysis, A Practical Introduction", CRC Press LLC, Boca Raton, 1998, pg 3.

3. Lu et al, "Measurement of creep compliance of solid polymers by nanoindentation", Mechanics of Time dependant materials, 7: 189-207, 2003.

4. Gama et al, "Hopkinson bar experimental technique: A critical review", Appl Mech Rev, vol 57, no 4, pp. 223-250 (July 2004).

5. Kolsky, H., "An Investigation of the Mechanical Properties of Materials at Very High Rates of Strain", *Proc. Roy. Phys. Soc.*, **B 62,** pp. 676-700 (1949)

6. Arlon Hunt, Michael Ayers, "A Brief History of Silica Aerogels", Ernest Orlando Lawrence Berkeley National Laboratory, http://eande.lbl.gov/ECS/aerogels/sahist.htm

7. Wang et al, "Cluster structure of Silica Aerogel Investigated by Laser Ablation", Nanostructured Materials, Vol. 10, No. 6. pp. 909-916.1998.

8. Barrett et al "Suitability of silica aerogel as a capture medium for interplanetary dust". In: Proc. Lunar Planet. Sci. Conf., pp. 203–212, 1992.

9. Domínguez et al, "Energy loss and impact cratering in aerogels: theory and experiment" , Icarus 172, 2004, pp 613-624.

10. Fricke, J.; Arduini-Schuster, M. C.; Buttner, D.; Ebert, H.-P.; Heinemann, U.; Hetfleisch, J.; Hummer, E.; Kuhn, J.; Lu, X. In *Thermal Conducti*V*ity 21*; Cremers, C. J., Fine, H. A., Eds.; Plenum Press: New York 1990; pp 235-245.

11. Pajonk, G. M. *Catal. Today* **1999**, *52*, 3-13.

12. Morris, C. A.; Anderson, M. L.; Stroud, R. M.; Merzbacher, C. I.; Rolison, D. R. Science 1999, 284, 622-624

13. Novak, B. M.; Auerbach, D.; Verrier, C. Chem. Mater. 1994, 6, 282-286

14. Yadav, S., Chichili, D. R., and Ramesh, K. T., "The Mechanical Response of a 6061-T6 Al/Al2O3 Metal Matrix Composite at High Rates of Deformation," Acta metall. Mater., 43, 4453–4464 (1995).

15. Franz, C. E., Follansbee, P. S., and Wright, W. J., "New Experimental Techniques with the Split Hopkinson Pressure Bar," in the 8th International Conference on High Energy Rate Fabrication, Pressure Vessel and Piping Division, ASME, I. Berman and J. W. Schroeder, eds., San Antonio, TX (1984).

16. Follansbee, P. S., "The Hopkinson Bar," Mechanical Testing, Metals Handbook, 9th ed., **8**, American Society for Metals, Metals Park, Ohio, 198–217 (1985).

17. Wu, X. J. and Gorham, D. A., "Stress Equilibrium in the Split Hopkinson Pressure Bar Test," J. PHYS. IV FRANCE, **7**, C3, 91–96 (1997).

18. Togami, T. C., Baker, W. E. and Forrestal, M. J., "A Split Hopkinson Bar Technique to Evaluate the Performance of Accelerometers," J. Appl.Mech., **63**, 353–356 (1996).

19. Chen, W., Zhang, B., and Forrestal, M. J., "A Split Hopkinson Bar Technique for Low-Impedance Materials," EXPERIMENTAL MECHANICS, **39**, 81–85 (1999).

20. Christensen, R. J., Swanson, S. R., and Brown, W. S., "Split- Hopkinson-Bar Tests on Rock Under Confining Pressure," EXPERIMENTAL MECHANICS, **29**, 508–513 (1972).

21. D.J.Frew,M.J.Forrestal W.Chen, "Pulse Shaping Techniques for Testing Brittle Materials with a Split Hopkinson Pressure Bar" , Experimental Experiments, 42, 93-106 (2002).

22. W.Chen, F.Lu and B.Zhou, "A Quartz-crystal-embedded Split Hopkinson Pressure Bar for the Soft Materials", Experimental Mechanics, 40, 1-6 (2000).

23. Radok, J.R.M, 'Visco-elastic stress analysis', Quarterly of Applied Mathematics 15, 1957, 198-202

24. www.measurementsgroup.com

25. Mechanical Measurements, Beckwith T.G, Buck N.L, 2nd edition, Addison-Welsley, 1969, Pg 292.

26. www.efunda.com.

27. Chen et al, "A Split Hopkinson bar Technique for low-impedance materials", Experimental Mechanics,1999, Vol 39, 81-85.

28. Davies EDH and Hunter SC ~1963!, The dynamic compression test of solids by the method of the split Hopkinson pressure bar ~SHPB!, *J.Mech. Phys. Solids* **11**, 155–179.

APPENDIX

```
%MATLAB PROGRAM FOR CALCULATING THE STRESS AND STRAIN DURING A SHPB
TEST
%%%%%%%%%%%%%%%%%%%%%%%%%%%%%%%%%%%%%%%%%%%%%%%%%%%%%%%%%%%%%%%%%%%%%%%
clc;clear;
fid=fopen('D:\Research\Aerogel\SHPB\New setup
_Rm136\Plots\incident_0.1c.dat','r');
[Data,counter]=fscanf(fid, '%g %g',[2 inf]);
fclose(fid);

ti=(Data(1,:));
ei=(2/(2.02*1800))*Data(2,:);%convert voltage to strain
fid=fopen('D:\Research\Aerogel\SHPB\New setup
_Rm136\Plots\reflected_0.1c.dat','r');
[Data,counter]=fscanf(fid, '%g %g',[2 inf]);
fclose(fid);

tr=(Data(1,:));
er=(2/(2.02*1800))*Data(2,:);
fid=fopen('D:\Research\Aerogel\SHPB\New setup
_Rm136\Plots\transmitted_0.1c.dat','r');
[Data,counter]=fscanf(fid, '%g %g',[2 inf]);
fclose(fid);
tt=(Data(1,:));
et=(2/(2.02*1800))*Data(2,:);

Ei=71344;Ds=0.65*25.4;ID=0.64*25.4;OD=0.75*25.4;Ls=0.1*25.4;Et=72000;
C=5065*10^3;
Ai=pi/4*OD^2;% Area of incident bar
As=pi/4*(Ds)^2;%Area of specimen
At=pi/4*((OD)^2-(ID)^2);%Area of Transmission bar
Ar=Ai/At;% Ratio of incident and transmission bar areas

figure(1);
plot(ti,ei,'r-',tr,er,'b-',tt,et,'g-');
ylabel('Strain');xlabel('Time (microseconds)');
legend('Incident','Reflected','Transmitted',1)
title('Strain Vs Time');
grid on;

incident_strain=[ti;ei];
 fid=fopen('D:\Research\Aerogel\SHPB\New setup
_Rm136\output\incident_strain.txt','w');
fprintf(fid,'%g %g\n',incident_strain);
fclose(fid);
reflected_strain=[tr;er];
 fid=fopen('D:\Research\Aerogel\SHPB\New setup
_Rm136\output\reflected_strain.txt','w');
fprintf(fid,'%g %g\n',reflected_strain);
fclose(fid);
transmitted_strain=[tt;et];
 fid=fopen('D:\Research\Aerogel\SHPB\New setup
_Rm136\output\transmitted_strain.txt','w');
fprintf(fid,'%g %g\n',transmitted_strain);
fclose(fid);

%%%%%%%%%% Specimen Strain Rate%%%%%%%%%%%
```

```
for i=1:length(tr)
    specimen_strain_rate(i)=(C/Ls)*((ei(i)*(1-Ar))-(er(i)*(1+Ar)));
end

figure(2);plot(tr,specimen_strain_rate,'r-');
ylabel('Strain rate');xlabel('Time (microseconds)');
title('Strainrate-Time');grid on;
 sr=[tr;specimen_strain_rate];
fid=fopen('D:\Research\Aerogel\SHPB\New setup
_Rm136\output\strain_rate_.txt','w');
fprintf(fid,'%g %g\n',sr);
fclose(fid);

%%%%%%%%%% Front force %%%%%%%%%%%%%%%%%%
for i=1:length(tr)
    strn(i)=ei(i)+er(i);
    front_force(i)=Ai*Ei*(strn(i));
end

%%%%%%%%%% Back Force %%%%%%%%%%%%%%%%%%%
for i=1:length(tt)
    back_force(i)=At*Et*et(i);
end

figure(3);plot(tr,front_force,'r-',tt,back_force,'b-');
ylabel('Force (N)');xlabel('Time (s)');
legend('Front','Back',1)
title('Equilibrium Check');grid on;

 ff=[tr;front_force];
 bf=[tt;back_force];
fid=fopen('D:\Research\Aerogel\SHPB\New setup
_Rm136\output\front_force.txt','w');
fprintf(fid,'%g %g\n',ff);
fclose(fid);
fid=fopen('D:\Research\Aerogel\SHPB\New setup
_Rm136\output\bck_force.txt','w');
fprintf(fid,'%g %g\n',bf);
fclose(fid);

%%%%%%%%%% Specimen Strain %%%%%%%%%%%%%%%
ss=0.0;
for i=1:length(tr)
   strain(i)=ss;
   if i<length(tr)
   ss=ss+(specimen_strain_rate(i)+specimen_strain_rate(i+1))*(ti(2)-
ti(1))/2;
   else
   ss=ss+specimen_strain_rate(i)*(ti(2)-ti(1));
   end
end
figure(4);plot(tr,strain,'r-');
ylabel('Strain');xlabel('Time (s)');
title('Strain-Time');grid on;
```

```
%%%%%%%%%% Specimen Stress %%%%%%%%%%%%%%%
    for i=1:length(tr)
        stress(i)=(At/As)*Et*et(i);
    end

figure(5); plot (strain,stress,'r-');
ylabel('Stress(MPa)');xlabel('strain');
title('Stress-strain Curve');grid on;

str=[strain; stress];
fid=fopen('D:\Research\Aerogel\SHPB\New setup
_Rm136\output\stress_strain.txt','w');
fprintf(fid,'%g %g\n',str);
fclose(fid);
```

VITA

Atul Ramesh Katti

Candidate for the Degree of

Master of Science

Thesis: CHARACTERIZATION AND MODELING OF THE THERM-MECHANICAL BEHAVIOR OF CROSSLINKED SILICA AEROGEL.

Major Field: Mechanical Engineering.

Biographical:

Personal Data:
Born in Hubli, India on 21st January, 1980, the son of Ramesh and Sumedha Katti

Education:
Received Bachelor of Engineering degree in Mechanical Engineering from University of Pune, India in august 2001. Completed the requirements for the Master of Science degree in Mechanical engineering at Oklahoma State University in December 2005.

Experience:

- Graduate Research Assistant in Mecahncial and Aerospace engineering Dept, Oklahoma State University, August 2002-Present.
- Teaching Assistant Assistant in Mecahncial and Aerospace engineering Dept, Oklahoma State University, Spring 2003.
- CAD/CAM Engineer in Shelik Industries from Jan 2002 to June 2002.

Professional Memberships:
ASME

Name: Atul Katti Date of Degree: December, 2005

Institution: Oklahoma State University Location: Stillwater, Oklahoma

Title of Study: CHARACTERIZATION OF THE THERMO-MECHANICAL BEHAVIOR OF CROSSLINKED SILICA AEROGEL.

Pages in Study: 81 Candidate for the Degree of Master of Science

Major Field: Mechanical Engineering.

Scope and Method of Study: Silica aerogels are highly porous materials. Applications are limited due to their brittle and hygroscopic nature. In an effort to increase the strength, Leventis developed a method to strengthen aerogels by crosslinking them with isocyanate.

Findings and Conclusions: DMA tests were conducted on the crosslinked silica aerogel samples revealed two glass transitions, one at 130 ^{o}C, indicating the major glass transition and the other at -50 ^{o}C indicating the secondary transition. The frequency scan data was shifted horizontally to get the storage modulus data for 25 decades. Nanoindentation tests were performed on CSA samples of various densities and the load depth curves were obtained. From this data the creep compliance curves and subsequently the relaxation moduli were obtained. The Load-depth curves indicate an increasing stiffness with the density. For the split Hopkinson bar tests perfect equilibrium and constant strain rate could not be achieved and hence the results serve only as estimates.

ADVISER'S APPROVAL: Dr. Hongbing Lu